Integration of geometry and analysis for the study of continuum-based airless tyres of planetary wheeled robots

Edoardo Samarini

Department of Mechanical Engineering,
Turin Polytechnic University,
Turin, 10129, Italy
Email: edoardo.samarini@gmail.com

Ahmed A. Shabana*

Department of Mechanical and Industrial Engineering,
University of Illinois at Chicago,
842 West Taylor Street, Chicago,
Illinois 60607, USA
Email: shabana@uic.edu
*Corresponding author

Emanuele Grossi

Exponent, 525 West Monroe Street,
Suite 1050, Chicago, IL 60661, USA
Email: egrossi@exponent.com

Aurelio Somà

Department of Mechanical Engineering,
Turin Polytechnic University,
Turin, 10129, Italy
Email: aurelio.soma@polito.it

Abstract: Because of the scientific challenges of space explorations, several space agencies are involved in the design of autonomous planetary surface exploration devices. Examples are *Mars rovers*, designed with the goal of collecting terrain information, including dust, soil, rocks, and liquids. The design of such sophisticated rovers can be enhanced by less reliance on trial-and-error process, building expensive physical models, and time-consuming experimental testing. Physics-based virtual prototyping contributes to an efficient and credible Mars rover designs. In this paper, a new flexible multibody system (MBS) rover model for planetary exploration is developed. Because the rover, a *wheeled robot*, must be designed to negotiate uneven terrains, the *airless wheels* must be able to adapt to different soil patterns and harsh operating and environmental conditions. In order to describe the airless-wheel complex geometry and capture its large deformations and rotations, the absolute nodal coordinate formulation (ANCF) finite elements are used.

A numerical study is performed to compare the ANCF kinematics and tractive force results with the results of the discrete brush tyre model, widely used in the vehicle-dynamics literature. Several simulation scenarios are considered, including a drop test and acceleration along a straight line. The numerical results obtained are verified using data published in the literature and are used to evaluate the accuracy and computational efficiency of the ANCF airless-tyre modelling approach.

Keywords: Mars rover; airless-tyre geometry; virtual prototyping; wheeled robots; ANCF; absolute nodal coordinate formulation; I-CAD-A; integration of computer-aided design and analysis; vehicle dynamics.

Reference to this paper should be made as follows: Samarini, E., Shabana, A.A., Grossi, E. and Somà, A. (xxxx) 'Integration of geometry and analysis for the study of continuum-based airless tyres of planetary wheeled robots', *Int. J. Vehicle Performance*, Vol. x, No. x, pp.xxx–xxx.

Biographical notes: Edoardo Samarini received his BS in Mechanical Engineering from the Polytechnic of Turin. He earned his MS in Mechanical Engineering from both the Polytechnic of Turin and the University of Illinois at Chicago in 2020. His research interests include modelling and simulation of mechanical systems as well as the design and analysis of ground vehicles.

Ahmed A. Shabana received his BSc from Cairo University in 1974, an MSc from Ain Shams University in 1978, and a PhD from the University of Iowa in 1982. He joined University of Illinois at Chicago (UIC) in 1983. He is author of a number of books which include *Dynamics of Multibody Systems* published by Cambridge University Press, and *Computational Dynamics* published by John Wiley and Sons. He is a UIC Distinguished Professor and the Richard and Loan Hill Professor of Engineering.

Emanuele Grossi received the MS in Mechanical Engineering from Polytechnic of Turin, Polytechnic of Milan, and University of Illinois at Chicago (2016), a PhD in Mechanical Engineering from University of Illinois at Chicago (2019). He is an engineering consultant at Exponent, where he applies his expertise to solve forensic engineering problems. He specialises in solid and fluid mechanics, nonlinear dynamics, durability analysis, and noise, vibration, and harshness analysis. As a certified vibration analyst, he is capable of conducting machinery vibration tests and analysing vibration data. His research interests cover computational mechanics, multibody dynamics, and virtual prototyping.

Aurelio Somà received the MS in Aeronautical Engineering (1989), PhD in Applied Mechanics (1993) at Politecnico di Torino. Since 2002 Full Professor, Chair of Machine Design at Politecnico di Torino. He coordinates several research projects with public and private funding Italian and European collaborative projects. His main research field of interest in the last years: numerical and experimental structural dynamics, identification, MEMS design modelling and experimental identification, simulation reliability and testing, energy harvesting dynamics and testing, railway dynamics vehicles and wheel rail contact, telescopic vehicle and hybrid-electric new working vehicle. He has published more than 250 scientific publications and 15 patents.

1 Introduction

Space exploration missions aimed at finding different forms of life elsewhere in the universe are one of the most ambitious scientific challenges. This is particularly true in the case of the exploration of Mars, which has the potential of providing biological signatures because of its past geological history. Future Mars space missions aim at searching for proof of life by analysing soil samples collected by a drill, directly mounted on wheeled rovers that function as robots. The wheeled-robots must be capable of negotiating rocky and uneven terrains that characterise the Mars planet. Consequently, accurate prediction of the kinematic and dynamic responses of the rover is critical for robust design, credible validation and verification, and science-based planning of such sophisticated machines. An important aspect that must be considered is the dynamic interaction between the soil and the rover wheels, which transmit the loads from the uneven and rocky terrain to other components of the wheeled robot.

Mars is the fourth planet in the solar system and has been recognised as the first candidate among other solar planets for space exploratory missions. The distance between the Earth and Mars varies depending on their orbital location; with an average distance of 225 million km. Because the two planets can be 401 million km apart, Mars rover launch missions are planned to take advantage of the closest relative position of the two planets. Mars extreme environmental conditions can potentially cause damage to mechanical devices, equipment, and machines. Among these conditions are the high-velocity dusty winds, low gravity, ultraviolet radiation, and significant daily variation in temperature and atmospheric pressure. The average of the wind velocity is 20 m/s and can rise to peaks of 25 m/s during dust storms. The atmospheric pressure, depending on the season, altitude and weather, varies from 7 to 9 mbar. Similarly, surface temperatures can vary widely between –143°C and 35°C; with the possibility of daily temperature variation in the range of 50°C. In general, Mars has a lower average temperature than the Earth because of its larger distance from the sun. Because of the Mars extreme environmental conditions and the Mars uneven and rocky terrain, the rover design has to be robust and reliable and must ensure successful completion of the scientific exploratory missions.

Regions of Mars which attract the highest scientific interest are characterised by very rough terrains. Mars poles, on the other hand, represent safer soil, despite the fact that the temperature could sink to –125°C. At this temperature level, martensitic steels become brittle, potentially causing failure of robot components made of this material, particularly when subjected to impacts or cyclic fatigue. Thermal stresses, resulting from high temperature variations during one day, can easily cause damage to the rover components. Furthermore, while negotiating uneven terrains might falsely appear easier because of the lower gravity of the planet, 3.711 m/s^2 as compared to the earth 9.81 m/s^2, one must keep in mind that such low gravity can result in loss of traction and inefficiencies in propelling forward the wheeled robot. Due to repeated high impulsive forces resulting from component-surface impacts, a dust storm can instantaneously damage and/or corrode the materials of the wheeled robot. Mechanical joints of the rover are particularly susceptible to malfunction because of dust, small particles, and debris that enter between jointed components, causing corrosion and abrasive wear, which can lead to joint failure.

In order to successfully complete space missions, the Mars rover is designed to satisfy several requirements (Poulakis et al., 2015). Among these requirements are the ability

to collect samples between two points up to 2 km apart; ability to cross the rough Martian terrain with a range of rock distributions; lateral and longitudinal gradeability of slopes up to 25°; ability to overcome obstacles up to 0.25 m height and cross crevasses with length of 0.15 m; ability to move at an average locomotion speed of 70 m/h; point-turn capability; and static stability of at least 40° in all directions.

2 Background, scope and contributions of this investigation

Figure 1 shows an image of the Mars rover model considered in this investigation. This wheeled robot interacts with the Mars uneven terrain using airless tyres, which provide support and serve as a vibration-isolation system. Because the wheeled robot does not have suspension springs, the airless tyres play an important role in defining the kinematic and dynamic characteristics of the rover. Airless tyres, such as the ones shown in Figure 2, are used because of their high durability that gives them an advantage over pneumatic tyres that are prone to punctures that can disable the rover and terminate its exploratory mission. Therefore, the design and integrity of the airless tyres are critical in ensuring successful completion of the rover mission.

Figure 1 Mars rover (see online version for colours)

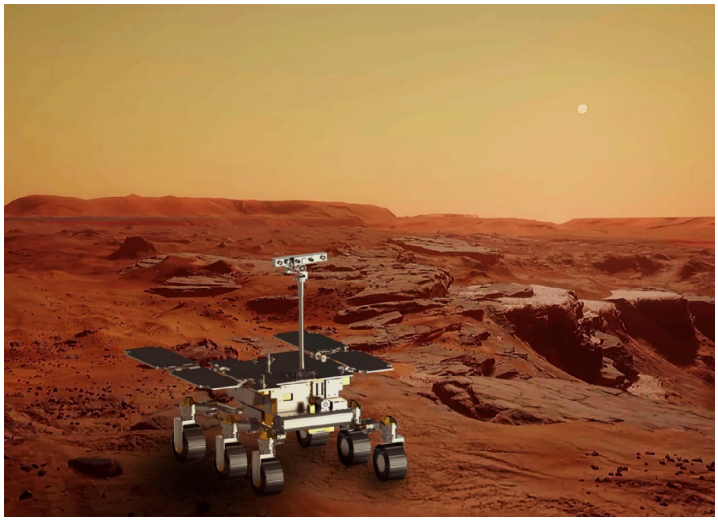

2.1 Discrete and continuum-based tyre models

Simple discrete tyre models may be adequate in investigations focused on the effect of the terrain inputs on the vehicle dynamics. However, such discrete simple models, which are often developed using spring-damper systems, are not adequate to study the tyre integrity and durability and do not correctly capture the high frequency variations in the tyre/terrain contact forces. While the discrete spring-damper models that produce discrete forces have been used in the literature to examine the motion of vehicles in response to terrain variations under different operating conditions, such simple models do not account for the tyre distributed elasticity and inertia, do not allow predicting strain distributions,

cannot be used to accurately determine the tyre distributed stresses and wear, and cannot be used to accurately describe and account for the complex tyre geometry particularly in the case of airless tyres. Continuum-based tyre formulations are required if these limitations are to be avoided. Such continuum-based tyre formulations allow for systematically accounting for the Mars extreme environmental conditions including the significant temperature variations. Another important design consideration is the accurate prediction of the *tractive forces* in the Mars low gravity environment. Use of continuum-based tyres also leads to a more realistic, larger, and conformal contact area as compared to the discrete tyre models.

Figure 2 Airless tyre (see online version for colours)

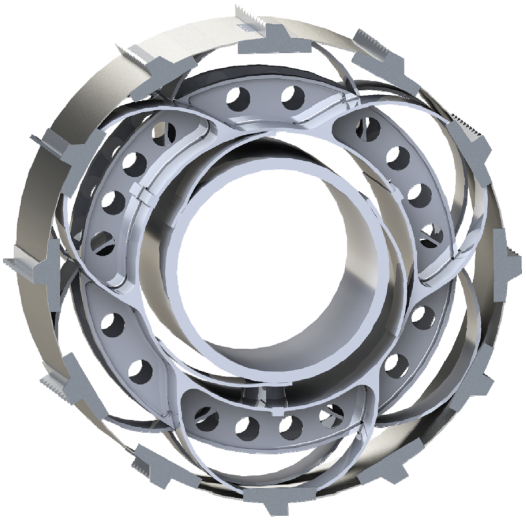

2.2 Scope of this Investigation

Accounting for the airless-tyre distributed inertia and elasticity is essential for developing high-fidelity multibody system (MBS) rover models. In this investigation, the absolute nodal coordinate formulation (ANCF) is used to develop both the *geometry* and *analysis meshes* (Hu et al., 2014; Fotland et al., 2019; Nachbagauer, 2014; Orzechowski and Fraczek, 2015; Shen et al., 2014; Ma et al., 2016, 2020; Obrezko et al., 2020; Liu et al., 2011; Shabana, 2018; Pappalardo et al., 2020; Wang, 2020; Yamano et al., 2020). ANCF elements have several desirable features, including constant mass matrix and zero Coriolis and centrifugal inertia forces. In this study, the airless tyres are modelled using fully parameterised ANCF plate elements, which allow for describing accurately the tyre geometry. In addition to using the continuum-based ANCF tyre formulation, a discrete brush-type tyre model that consists of rigid bodies connected by springs and dampers is used for the purpose of comparison and verification (Gipser, 2005; Lugner et al., 2005; Pacejka, 2006). However, this simpler discrete tyre modelling approach, as previously mentioned, is not suited for capturing geometric details as well as geometric and material nonlinearities that cannot be ignored in the planning of critical and costly space missions. The second approach is based on the ANCF *geometry/analysis method* which allows alleviating the limitations of the discrete tyre models. The two different tyre models

considered in this study are shown in Figure 3. The ANCF tyre formulation was previously used in the literature to develop physics-based tyre models (Patel et al., 2016; Pappalardo et al., 2017; He et al., 2017; Grossi et al., 2019). An ANCF wheel model for Mars exploration rover was recently proposed by Sivo et al. (2019), who developed a detailed FE wheel mesh and performed a nonlinear static analysis in order to characterise the wheel stiffness properties. In the work of Sivo et al., however, no MBS model for the Mars rover was developed, and the study was focused mainly on the stiffness characterisation of the tyre.

The goal of this investigation is to develop a new Mars rover MBS virtual prototyping model that includes tyres with distributed inertia and elasticity. The model developed in this study is verified using results previously published in the literature, including some of the results reported by Sivo et al. (2019). The newly developed MBS dynamic rover model allows predicting the tyre deformations, can be used in different motion scenarios, can be integrated with general MBS algorithms that systematically construct and numerically solve the rover differential/algebraic equations (DAEs), and can be generalised in future investigations to study the effect of the Mars environmental conditions including the effect of the significant temperature variations.

Figure 3 Brush and ANCF tyre models

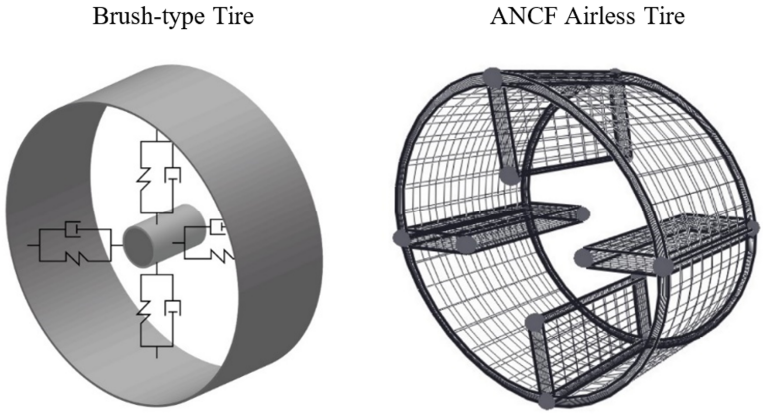

2.3 Contributions of this Investigation

Airless wheels are often used for space robots in order to avoid serious problems and rover malfunction that can result from using pneumatic tyres, which are prone to puncturing and are less durable in harsh environmental conditions. Nonetheless, airless wheels often have complex geometries that make their virtual analysis and integration with virtual rover MBS models more challenging. Conventional finite element (FE) formulations have well-known limitations in the analysis of tyres and other soft components with complex geometries. Recent investigations have demonstrated that conventional Lagrangian FE formulations based on co-rotational and incremental procedures do not lead to accurate results in case of large displacements of soft and fluid materials (Ma et al., 2020; Obrezko et al., 2020; Shabana and Zhang, 2020). This lack of accuracy is attributed to the conventional FE kinematics and to adopting the co-rotational solution procedure widely used in commercial FE software. Furthermore,

such conventional FE formulations are not related by a linear mapping to the computational geometry methods used in the computer-aided-design (CAD) software. In the CAD software, basis splines (B-splines) and non-uniform rational B-splines (NURBS) are used to develop the solid-model geometry (Piegl and Tiller, 1997; Farin, 2002; Rogers, 2001; Gallier, 2011; Goetz, 1970; Kreyszig, 1991). The airless tyres of space wheeled-robots have complex geometry and are subjected to environmental and operating conditions that necessitate use of geometrically-accurate formulations capable of capturing large rotational motion as well as large deformations. These formulations must also allow for systematic integration of the airless-tyre meshes with computational MBS algorithms designed to solve the governing DAEs of the wheeled robot.

In this study, a new computational approach is used for the nonlinear analysis of the Mars rover system. This approach allows developing detailed flexible MBS rover models that include continuum-based airless tyres. In the proposed computational framework, ANCF fully-parameterised plate elements are used to develop a unified tyre *geometry/analysis mesh*. The main contributions of this study can be summarised as follows:

- A new detailed MBS rover model with airless tyres, that have distributed inertia and elasticity, is developed and integrated with a computational MBS algorithm designed to systematically construct and numerically solve the system DAEs.
- The rover-tyre geometry and analysis mesh are developed using eight ANCF fully-parameterised plate elements that take into account structural discontinuities. This feature is important in the definition of the geometry of the airless tyres. It is demonstrated that such coarse mesh is sufficient to correctly capture the tyre geometry and flexural response.
- The concept of the ANCF reference node is used to assemble the six tyres of the rover at a preprocessing stage. That is, all the rover tyres at the geometry and analysis stages are represented by one FE mesh despite the fact that these tyres can have arbitrarily large displacements, including finite rotations, with respect to each other.
- An approach for the prediction of the *tractive forces* of the airless-tyre rover is outlined in this study. The contact forces are evaluated by defining a point mesh on the ANCF plate elements. This point mesh is used to determine the tyre/terrain contact patch leading to a more realistic representation of the contact geometry and tractive forces. The results obtained in this study show that the continuum-based tyre model can capture the oscillations in the airless-tyre tangential friction forces.
- Using the nonlinear MBS approach adopted in this investigation, a study is performed to compare between rover models developed using the discrete brush-type and continuum-based ANCF tyre models. The results obtained in this investigation are verified by comparing with numerical data published in the literature. The advantages and limitations of each tyre model are discussed.

This paper is organised as follows. Section 3 discusses the main features of the Mars rover used in this investigation and explains its main components that make the rover function as a wheeled robot. Section 4 describes the continuum-based ANCF tyre used in this study and explains wheel-design issues that are considered for the

Mars-exploration vehicle. The ANCF large-deformation analysis, ANCF treatment of structural discontinuities, and ANCF concept of the *reference node* are among the topics discussed in Section 4. Section 5 discusses the traction and tyre contact force models used in this study and describes the displacement field of the fully-parameterised ANCF finite element used in this investigation. The form of the constrained dynamic equations of motion used in the computational algorithm employed to solve the rover equations is presented in Section 6. Section 7 presents the two rover models developed in this investigation; the discrete brush-type tyre model and the continuum-based ANCF airless tyre model. After verification of the results by comparing with the results available in the literature, nonlinear dynamic simulations of the rover are performed and the results of different models are compared. Section 8 presents summary and conclusions of the study.

3 Mars wheeled-robots and MBS algorithms

In order to avoid the costly and time-consuming process of building physical prototypes which cannot be always used to conveniently experiment with design modifications, *virtual prototyping* is becoming the preferred approach for developing the initial designs. Virtual prototyping allows for easily experimenting with different design parameters and configurations and can be used to significantly reduce reliance on physical prototyping and experimentation.

3.1 MBS algorithms

MBS algorithms, in particular, play a significant role in the design of physics and engineering systems that consist of interconnected bodies that experience arbitrarily large relative displacements and rotations. While it is difficult to reproduce the Martian environmental conditions on Earth when heavily relying on physical prototyping, virtual prototyping allows changing the environmental conditions over a wide parameter range without the need for extensive, costly, and error-prone experimentation. For these reasons, the initial design, testing, and planning of a Mars wheeled-robot are currently being made by first developing and analysing reliable and accurate physics-based virtual models using *MBS algorithms*. These algorithms allow developing detailed models that include interconnected rigid and flexible bodies, for performing computer simulations for different motion scenarios and operating and loading conditions, and for studying the interaction between the tyres and soil. Among the main concerns in the design of Mars wheeled-robots are the static stability of the vehicle over steep slopes and the ability to negotiate a terrain characterised by rocks and crevasses. With regard to the terrain unevenness and discontinuities, practicing engineers and researchers worked on the design of certain types of tyres that can experience large deformations to provide the flexibility needed for successfully negotiating terrains with different irregularities, discontinuities, and material properties. The goal is to achieve higher degree of mobility and obtain the desired performance when the robot negotiates both soft soils (sands, fine granular materials) and rigid surfaces (rocks, coarse granular materials). The development of a reliable and efficient MBS rover model, which is among the goals of this study, should represent one of the first steps in planning a Mars space mission. The conclusions based on the numerical results of the virtual experimentation with the

MBS model can provide valuable information and can serve as a guide in the design of the wheeled robot as well as in the space mission planning.

Figure 4 Bogie electro-mechanical assembly (BEMA) subsystem (see online version for colours)

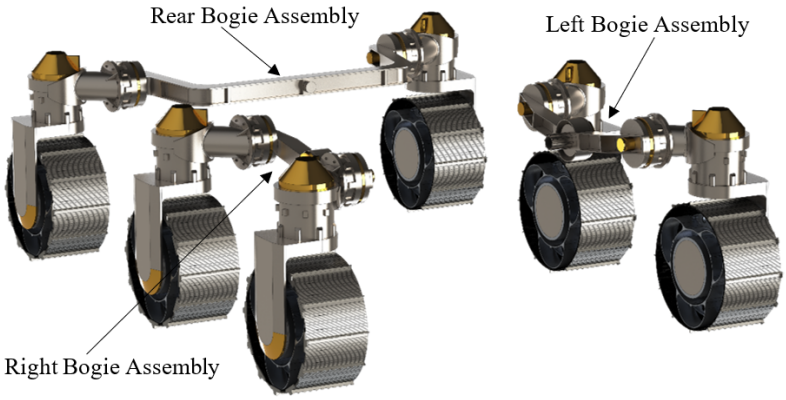

Figure 5 Different actuator positions (see online version for colours)

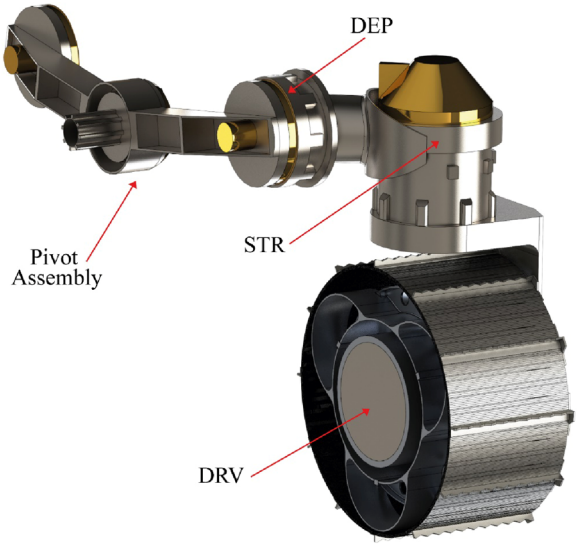

3.2 Rover structure

The Mars rover considered in this investigation is a 6-wheel triple-bogie vehicle, as shown in Figure 1. The model includes the principal body, on which the drill, sensing, and control equipment are mounted. The system is designed to be autonomously controlled with bogie electro-mechanical assembly (BEMA), which provides the desired mobility as illustrated in Figure 4. The BEMA $6 \times 6 \times 6 + 6$ locomotion formula provides good stability of the overall rover when negotiating different rough terrains. This formula, which gives a clear picture of the vehicle topology, implies 6-supporting wheels, 6-driven wheels, 6-steered wheels, plus 6-deployment drivers. Each bogie structure consists of two metallic wheels and 18 actuators (six *drive* (DRV), six *steering*

(STR), and six *deployment* (DEP)), as shown in Figure 5. The suspension and locomotion elements are designed as thin-walled, riveted box structures made of titanium alloy, in order to maximise the stiffness and minimise the mass. The mobility subsystem is composed of six identical motor modules, placed symmetrically with respect to the centre of mass. These units allow performing drive and turn-on spot manoeuvres, as well as powering the vehicle to drive along different terrains and climb over rocks. Each module is equipped with three different independent motors that can be actuated autonomously in order to steer, control the pitch angle, and/or provide the power required for moving the rover wheels over different terrains.

4 Continuum-based airless tyres

In space wheeled-robots, airless tyres are used for their proven durability and for avoiding pneumatic-tyre punctures that can result in early termination of costly space missions. Nonetheless, virtual-prototyping investigations of airless tyres have been limited because of their complex geometries that need to be modelled accurately and because of the need for an analysis approach that allows capturing accurately the tyre large deformations. In this study, a unified airless-tyre geometry/analysis mesh is developed and used in the computer simulations of the MBS wheeled-robot model. Such a model demonstrates the value of the integration of computer-aided design and analysis (I-CAD-A) in developing detailed virtual prototyping models for space applications and in avoiding costly conversion of CAD solid models to analysis meshes (Shabana, 2019; Pappalardo et al., 2020).

4.1 Airless-tyre geometry and Mars terrain

The surface of Mars can be extremely irregular because of crevasses and different types of rocks that cover the soil. Consequently, the robot wheels must be able to adapt and deform in a manner that allows the rover to successfully negotiate obstacles which can have different and irregular shapes. This essential feature plays a key role in the overall rover stability and ability to safely travel over rough terrains.

Several studies have been focused on the design of various types of wheels with the goal of increasing the soil-contact patch for better force distribution, decreasing the ground pressure to reduce the contact stresses and minimise wear, and providing impact-load absorption capability to avoid severe and unwanted vibrations (Knuth et al., 2012; Johnson et al., 2015). The wheel geometry considered in this study is similar to the geometry proposed by Sivo et al. (2019). Figure 6 shows the principal components of this complex structure, which can be divided into *external tyre*, *outer hub*, and *inner hub*. The external tyre, in which 12 *grousers* spaced at 30° are installed for enhancing traction capability, is connected to the outer hub by nine operational springs. These springs are divided into six outer springs and three inner springs, mounted out of phase in order to reduce the radial stiffness variation. The outer hub is connected to the inner hub through a cone and impact springs, allowing for relative rotation and displacement between the two hubs. For the purpose of verification of the wheel model developed in this study, the displacement-force curve obtained by Sivo et al. (2019) and shown in Figure 7 is used. The different curves in this figure, obtained using nonlinear static analysis, represent the stiffness characteristics of the wheel at different circumferential positions.

Figure 6 Wheel details (see online version for colours)

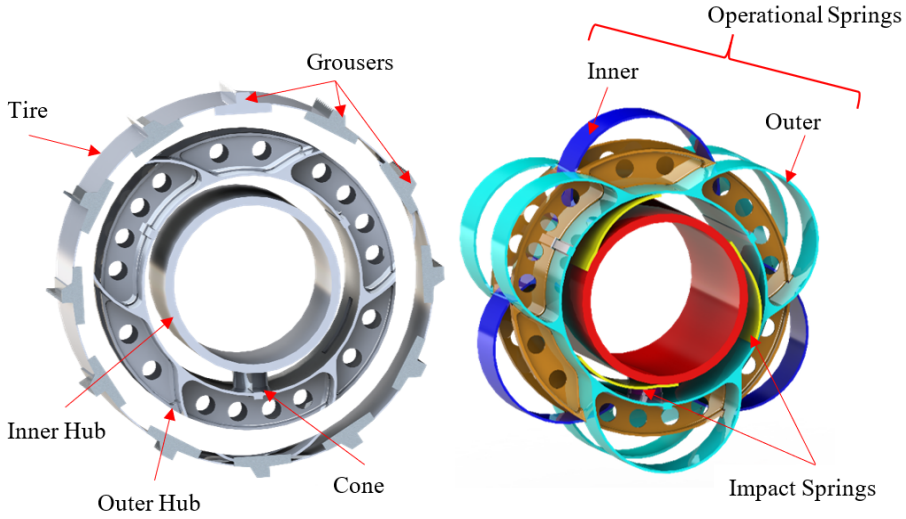

Figure 7 Deformation-force curves (Sivo et al., 2019) (see online version for colours)

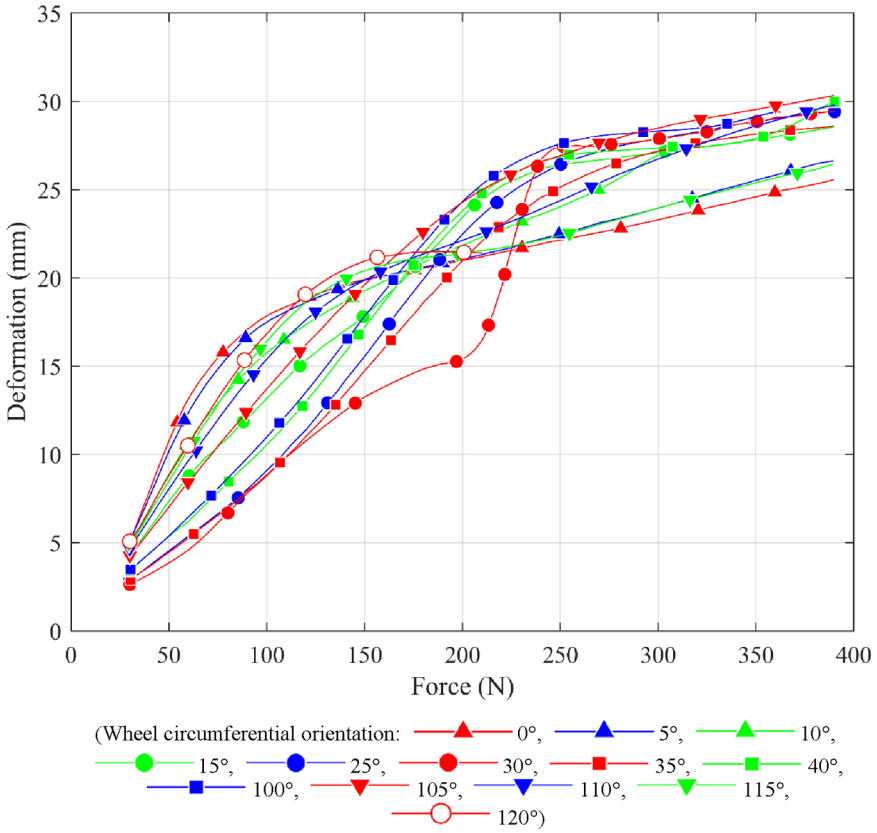

4.2 Unified ANCF geometry/analysis mesh

ANCF finite elements can be used to develop unified and accurate geometry/analysis meshes for the Mars-rover airless tyres, thereby avoiding the costly and time consuming conversion of solid models to analysis meshes. In this investigation, fully-parameterised ANCF plate elements are used to create the geometry/analysis mesh of the airless tyres. These elements allow for describing an arbitrary stress-free reference-configuration geometry by changing the length and orientation of the nodal position-gradient vectors. A coarse mesh with only four radial elements, as shown in Figure 8, was found to be sufficient to characterise the tyre flexural response. Fully-parameterised ANCF finite elements, which have a complete set of position-gradient vectors, also allow describing geometric discontinuities that may include T- and V-sections. Furthermore, as previously mentioned, ANCF elements allow avoiding geometry distortions that result from converting CAD solid models into FE analysis meshes (Grossi et al., 2019). The complex airless-tyre shape can be obtained by modifying the position-vector gradients at the mesh nodal points at a preprocessing stage. That is, the overall element- and mesh-geometry changes as well as local shape manipulations can be conveniently made using the vector of nodal coordinates in the stress-free reference configuration.

Figure 8 Airless tyre mesh developed using ANCF fully-parameterised plate elements: radial elements (red), circumferential elements (black) (see online version for colours)

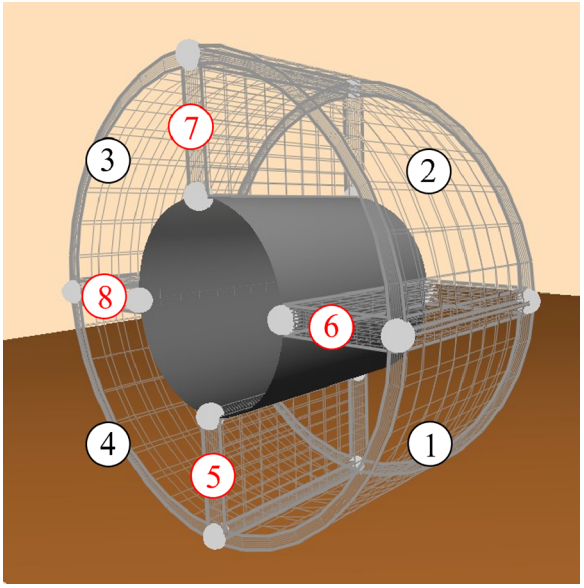

In this study, as shown in Figure 9, the wheel geometry is described using three different sets of coordinates or parameters, namely $\mathbf{x}=\begin{bmatrix}x_1 & x_2 & x_3\end{bmatrix}^{\mathrm{T}}$ associated with the straight configuration, $\mathbf{X}=\begin{bmatrix}X_1 & X_2 & X_3\end{bmatrix}^{\mathrm{T}}$ associated with the stress-free reference configuration, and $\mathbf{r}=\begin{bmatrix}r_1 & r_2 & r_3\end{bmatrix}^{\mathrm{T}}$ associated with the current deformed configuration. The matrix of position-vector gradients is defined as $\mathbf{J}=\partial\mathbf{r}/\partial\mathbf{X}=\left(\partial\mathbf{r}/\partial\mathbf{x}\right)\left(\partial\mathbf{x}/\partial\mathbf{X}\right)=\mathbf{J}_e\mathbf{J}_o^{-1}$, where $\mathbf{J}_o=\partial\mathbf{X}/\partial\mathbf{x}$, $\mathbf{J}_e=\partial\mathbf{r}/\partial\mathbf{x}$. The Green-Lagrange strain tensor is defined as $\boldsymbol{\varepsilon}=\left(1/2\right)\left[\left(\mathbf{J}_o^{-1}\right)^{\mathrm{T}}\mathbf{J}_e^{\mathrm{T}}\mathbf{J}_e\mathbf{J}_o^{-1}-\mathbf{I}\right]$, where $\mathbf{I}$ is the 3×3

identity matrix. The straight, current-deformed, and stress-free reference configurations are associated with three different volumes V, v, and V_o, respectively. The relationships between these volumes are $dv = JdV_o$, $dV_o = J_o dV$, and $dv = J_e dV$, where J, J_o, and J_e are the determinants of the gradient matrices $\mathbf{J}$, $\mathbf{J}_o$, and $\mathbf{J}_e$, respectively.

The global position vector of an arbitrary point on an ANCF finite element is defined as $\mathbf{r}(\mathbf{x},t) = \mathbf{S}(\mathbf{x})\mathbf{e}(t)$ where $\mathbf{x} = [x_1 \quad x_2 \quad x_3]^{\mathbf{T}} = [x \quad y \quad z]^{\mathbf{T}}$ is the vector of the element spatial coordinates, t is time, $\mathbf{S}$ is the element shape function matrix, and $\mathbf{e}$ is the vector of element nodal coordinates. In the case of the fully-parametrised plate element, the vector of nodal coordinates of each element can be written as $\mathbf{e}(t) = \left[\mathbf{e}^{1^{\mathrm{T}}} \quad \mathbf{e}^{2^{\mathrm{T}}} \quad \mathbf{e}^{3^{\mathrm{T}}} \quad \mathbf{e}^{4^{\mathrm{T}}}\right]^{\mathbf{T}}$, where $\mathbf{e}^k = \left[\mathbf{r}^{k^{\mathrm{T}}} \quad \left(\partial \mathbf{r}^k / \partial x\right)^{\mathbf{T}} \quad \left(\partial \mathbf{r}^k / \partial y\right)^{\mathbf{T}} \quad \left(\partial \mathbf{r}^k / \partial z\right)^{\mathbf{T}}\right]^{\mathrm{T}}$, $k = 1,2,3,4$. The vector $\mathbf{e}(t)$ can be written in terms of the nodal displacement vector $\mathbf{e}_d(t)$ as $\mathbf{e}(t) = \mathbf{e}_o + \mathbf{e}_d(t)$, where $\mathbf{e}_o$ is the vector of coordinates in the reference configuration which can be used to define complex stress-free reference configuration plate-mesh geometries.

Figure 9 Three geometry configurations (see online version for colours)

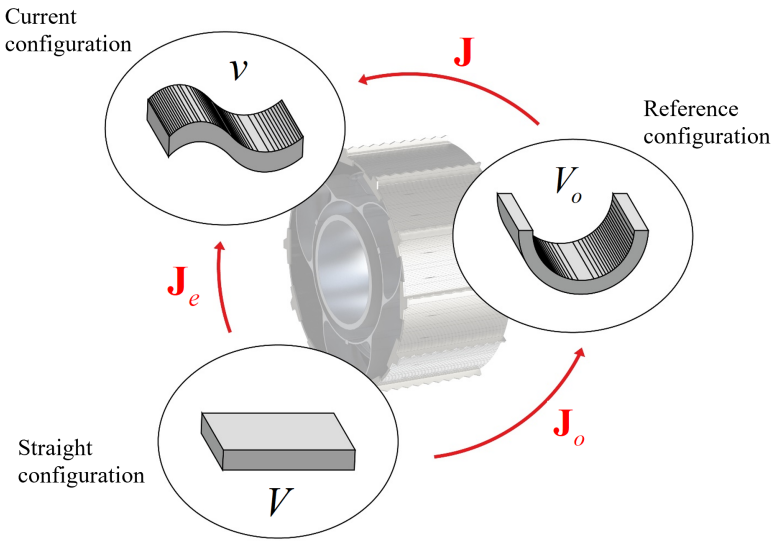

4.3 Structural discontinuities

The ANCF airless-tyre geometry considered in this paper is characterised by structural discontinuities between radial and circumferential elements, as shown in Figure 10. At a point or node of discontinuity, the coordinate lines (parameters) are not continuous. Examples of these discontinuities are T- and V-sections, as previously mentioned. At a discontinuity node, two different plate elements have two different sets of gradient coordinates. In order to model the structural discontinuity, the approach adopted by Patel et al. (2019) is used in this investigation. The idea is to define the element nodal coordinates in a *structure coordinate system* common to all elements of the FE mesh. In this case, the nodal coordinate vector $\mathbf{e}^i$ of element i can be defined in the

structure coordinate system using the gradient transformation $\mathbf{T}^i$ as $\mathbf{e}^i = \mathbf{T}^i\mathbf{p}^i$, where $\mathbf{p}^i$ is the vector of element nodal coordinates defined along the coordinate lines of the structure coordinate system. It is important to emphasise that the transformation matrix $\mathbf{T}^i$ is not in general an orthogonal matrix; it is the matrix obtained by defining the relationship between two different sets of gradient vectors that are tangent to two different sets of coordinate lines (parameters). Using this approach, the connectivity conditions at a discontinuity node k between two elements i and j can be written using the linear algebraic equations $\mathbf{C}^k\left(\mathbf{p}^i, \mathbf{p}^j\right) = \mathbf{0}$, where $\mathbf{p}^i$ and $\mathbf{p}^j$ are, respectively, the nodal coordinates of the two elements i and j defined in a common structure coordinate system. The constraint Jacobian matrix between the two elements i and j that share a common node k, can then be defined as

$$\mathbf{C}^k_{\mathbf{p}} = \begin{bmatrix} \mathbf{C}^k_{\mathbf{p}^i} & \mathbf{C}^k_{\mathbf{p}^j} \end{bmatrix} = \begin{bmatrix} \partial\mathbf{C}^k/\partial\mathbf{p}^i & \partial\mathbf{C}^k/\partial\mathbf{p}^j \end{bmatrix} = \begin{bmatrix} \mathbf{S}^{ki}\mathbf{T}^{ki} & -\mathbf{S}^{kj}\mathbf{T}^{kj} \\ \mathbf{S}^{ki}_x\mathbf{T}^{ki} & -\mathbf{S}^{kj}_x\mathbf{T}^{kj} \\ \mathbf{S}^{ki}_y\mathbf{T}^{ki} & -\mathbf{S}^{kj}_y\mathbf{T}^{kj} \\ \mathbf{S}^{ki}_z\mathbf{T}^{ki} & -\mathbf{S}^{kj}_z\mathbf{T}^{kj} \end{bmatrix} \tag{1}$$

where $\mathbf{p} = \begin{bmatrix} \mathbf{p}^{i^{\mathrm{T}}} & \mathbf{p}^{j^{\mathrm{T}}} \end{bmatrix}^{\mathrm{T}}$, $\mathbf{T}^{ke}$ is a partition of the transformation matrix $\mathbf{T}^e$ of element $e, e = i, j$, associated with node k; $\mathbf{S}^{ke}_\alpha = \partial\mathbf{S}^{ke}/\partial\alpha$, $\alpha = x, y, z$, and $\mathbf{S}^{ke}$ is the shape function matrix of element e evaluated at point or node k. Because the Jacobian matrix $\mathbf{C}^k_{\mathbf{p}^e}$ is constant, a constant velocity transformation matrix can be developed for the entire mesh and used to perform a standard FE assembly. This assembly process eliminates the dependent variables at the discontinuity node at a preprocessing stage.

Figure 10 Airless-tyre structural discontinuities (see online version for colours)

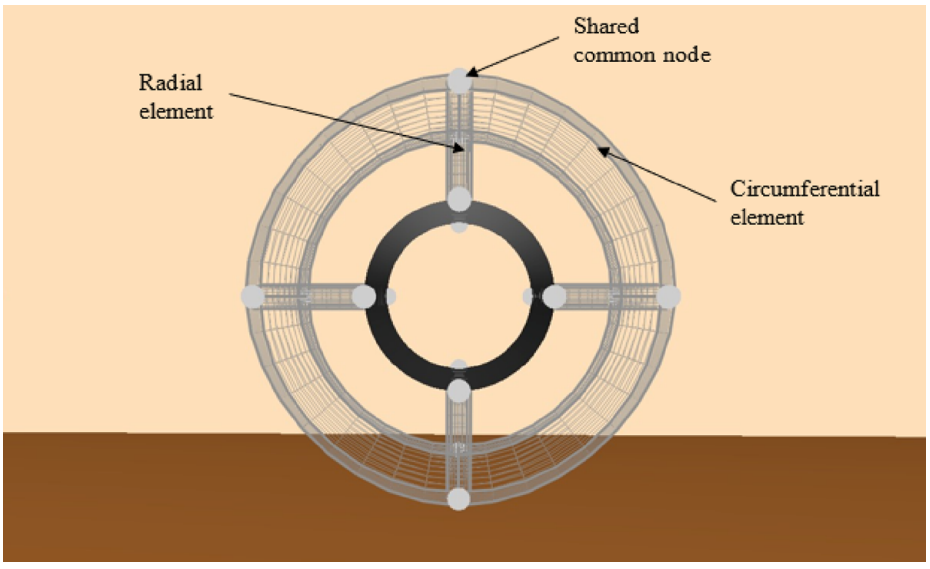

4.4 Airless-tyre assembly

The Mars rover considered in this study has six wheels; each of which can have arbitrarily large displacements including finite rotations. The ability to have this large displacement allows the rover to negotiate, and if necessary, climb very rough terrains that characterise the Mars soil. Because ANCF finite elements can describe arbitrarily large displacements, one *geometry/analysis mesh* can be developed to include the six wheels despite the fact that these wheels can have independent and large displacement with respect to each other. Such a geometry/analysis mesh defines the wheel assembly; and such an assembly, which can be performed at a preprocessing stage, can also include the wheel hubs, axles, and control arms. Using this ANCF assembly procedure, the dependent variables can be eliminated at a preprocessing stage; contributing to reduction in the model dimensionality. This new geometry/analysis mesh can be developed using the concept of the *ANCF reference node* (Shabana, 2014, 2015). It is, which is fundamentally different from the rigid-body element (RBE) used in commercial FE software, as previously discussed in the literature.

AQ1: Please check if the highlighted amended correction is ok.

As previously mentioned, the ANCF reference node (ANCF-RN), used in the rover hub/wheel assembly, allows defining general connectivity conditions at a preprocessing stage thus eliminating dependent variables resulting from imposing RN constraint equations. While the ANCF-RN is not associated with any particular element of the mesh, it has its own coordinates which consist of one position vector and three position-gradient vectors. In order to connect the ANCF reference node, referred to using the superscript r, with another mesh nodes, referred to using the superscript k, all or a subset of the following linear algebraic constraints can be applied at a preprocessing stage, depending on the number and type of conditions to be imposed:

$$\begin{aligned} &\mathbf{r}^k - \mathbf{r}^r = x^k \mathbf{r}_x^r - y^k \mathbf{r}_y^r - z^k \mathbf{r}_z^r \\ &\begin{bmatrix} \mathbf{r}_x^k & \mathbf{r}_y^k & \mathbf{r}_z^k \end{bmatrix} = \begin{bmatrix} \mathbf{r}_x^r & \mathbf{r}_y^r & \mathbf{r}_z^r \end{bmatrix} \mathbf{J}^{kr}, \qquad k = 1,\ldots,m_r \end{aligned} \tag{2}$$

where $\mathbf{r}$ represents the global position vector of the node; x^k, y^k, and z^k are the Cartesian coordinates of the tyre interface node k in the reference configuration with respect to the reference node r; $\mathbf{J}^{kr}$ is a constant matrix of position gradients defined in the reference configuration by the equation $\mathbf{J}^k = \mathbf{J}^r \mathbf{J}^{kr}$ in which the matrix $\mathbf{J}^i$ contains the position vector gradients associated with the node $i = k, r$; and m_r is the total number of nodes that have constraints with the reference node. The reference node used in this investigation for the wheel assembly is shown in Figure 11. A reference node can be used to represent a rigid hub or axle as discussed in the literature.

4.5 ANCF finite element

In order to evaluate the tyre/terrain interaction forces, a point grid is defined on the outer surface of the tyre and is used to search for the contact points using a point-search algorithm. The tyres are discretised using fully-parameterised ANCF plate elements. The displacement field of an element j can be written as $\mathbf{r}^j\left(\mathbf{x}^j, t\right) = \mathbf{S}^j\left(\mathbf{x}^j\right)\mathbf{e}^j\left(t\right)$, where $\mathbf{S}^j$ and $\mathbf{e}^j$ are, respectively, the element shape function matrix and the vector of element nodal coordinates. The element shape function matrix is given by

$$\mathbf{S}^j = \begin{bmatrix} s_1\mathbf{I} & s_2\mathbf{I} & s_3\mathbf{I} & s_4\mathbf{I} & s_5\mathbf{I} & s_6\mathbf{I} & s_7\mathbf{I} & s_8\mathbf{I} \\ s_9\mathbf{I} & s_{10}\mathbf{I} & s_{11}\mathbf{I} & s_{12}\mathbf{I} & s_{13}\mathbf{I} & s_{14}\mathbf{I} & s_{15}\mathbf{I} & s_{16}\mathbf{I} \end{bmatrix} \tag{3}$$

where $\mathbf{I}$ is the 3 × 3 identity matrix and the shape functions s_i, i = 1, 2, …, 16, are defined as follows:

$$\left.\begin{aligned} &s_1 = -(\xi-1)(\eta-1)\left(2\eta^2-\eta+2\xi^2-\xi-1\right), s_2 = -a\xi(\xi-1)^2(\eta-1), s_3 = -b\eta(\eta-1)^2(\xi-1), \\ &s_5 = \xi\left(2\eta^2-\eta-3\xi+2\xi^2\right)(\eta-1), s_6 = -a\xi^2(\xi-1)(\eta-1), s_4 = t\varsigma(\xi-1)(\eta-1), \\ &s_7 = b\xi\eta(\eta-1)^2, s_8 = -t\xi\varsigma(\eta-1), s_9 = -\xi\eta\left(1-3\xi-3\eta+2\eta^2+2\xi^2\right), s_{10} = a\xi^2\eta(\xi-1), \\ &s_{11} = b\xi\eta^2(\eta-1), s_{12} = t\xi\eta\varsigma, s_{13} = \eta(\xi-1)\left(2\xi^2-\xi-3\eta+2\eta^2\right), s_{14} = a\xi\eta(\xi-1)^2, \\ &s_{15} = -b\eta^2(\xi-1)(\eta-1), s_{16} = -t\eta\varsigma(\xi-1) \end{aligned}\right\} \tag{4}$$

and $\xi = x_1^j/a$, $\eta = x_2^j/b$, and $\varsigma = x_3^j/t$, and t is the element thickness. The element has four nodes. Each node k has 12 coordinates: three translational coordinates $\mathbf{r}^{jk}$, and nine gradient coordinates defined by the three vectors $\mathbf{r}_{x_1}^{jk}$, $\mathbf{r}_{x_2}^{jk}$, and $\mathbf{r}_{x_3}^{jk}$. Therefore, the element has 48 nodal coordinates, which can be written in a vector form as

$$\mathbf{e}^j = \left[\mathbf{e}^{j1^{\mathrm{T}}} \quad \mathbf{e}^{j2^{\mathrm{T}}} \quad \mathbf{e}^{j3^{\mathrm{T}}} \quad \mathbf{e}^{j4^{\mathrm{T}}}\right]^{\mathrm{T}} \tag{5}$$

In this equation, $\mathbf{e}^{jk} = \left[\mathbf{r}^{jk^{\mathrm{T}}} \quad \mathbf{r}_{x_1}^{jk^{\mathrm{T}}} \quad \mathbf{r}_{x_2}^{jk^{\mathrm{T}}} \quad \mathbf{r}_{x_3}^{jk^{\mathrm{T}}}\right]^{\mathrm{T}}$.

Figure 11 ANCF reference node (see online version for colours)

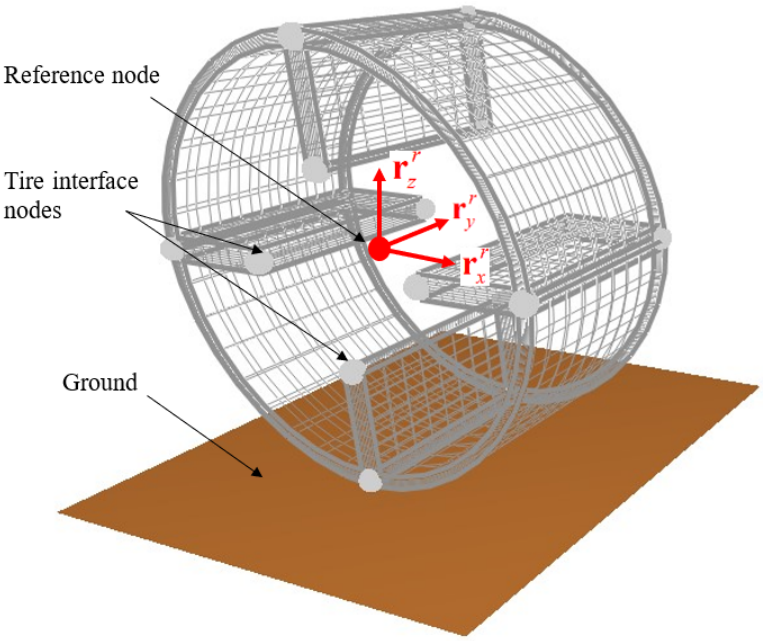

5 Traction and tyre contact forces

The wheel/soil interaction represents one of the main concerns when performing the MBS computer simulations of the rover system. In this section, the tyre contact and traction force model used in this investigation are discussed.

5.1 Tyre contact algorithm

In order to determine the tyre/terrain contact points, the following procedure is used:

- A broad phase collision-detection check is made to determine the distance of the tyre finite elements from the ground in order to focus the contact search on a smaller number of elements.
- On the elements, which can come in contact with the ground, a point grid on the outer surface of the element is defined. This grid defines a sufficient number of points necessary for an accurate distribution of the contact forces.
- The global position and gradient vectors of the grid points are determined and used to check whether or not these points are in contact with the ground. The position gradients in the element tangent plane are used to determine the normal to the surface at the grid point.
- If a point on the finite element is in contact with the ground, the normal contact force is computed using a penalty force model which has stiffness and damping coefficients provided by the user.
- The relative velocities between the element grid points and the ground are computed. If the tangential relative velocity at a point is different from zero, a tangential friction force.
- The normal and tangential contact forces define the contact-force vector which is used to determine the generalised contact forces associated with the plate element nodal coordinates. Since multiple contact points may exist, the ANCF generalised forces must account for the forces at all the contact points on the finite elements.

Following a procedure similar to the one used by Patel et al. (2016), the penalty contact force vector is defined as $\mathbf{f}_c = \mathbf{f}_n + \mathbf{f}_t$ where $\mathbf{f}_t$ is the tangential friction force and $\mathbf{f}_n$ is the normal contact force. In this investigation, the normal contact force is defined as $\mathbf{f}_n = \left(k_n\delta + c_n\dot{\delta}\right)\mathbf{n}$, where k_n and c_n are, respectively, penalty stiffness and damping coefficients, δ is the penetration, and $\mathbf{n} = \left(\mathbf{r}_{x_1} \times \mathbf{r}_{x_2}\right) \Big/ \left|\mathbf{r}_{x_1} \times \mathbf{r}_{x_2}\right|$ is the unit normal to the surface at the contact point. If the tangential relative velocity at the contact point is different from zero, the tangential friction force is defined as $\mathbf{f}_t = -\mu_t \left|\mathbf{f}_n\right| \mathbf{t}$, where μ_t is the friction coefficient and $\mathbf{t}$ is a unit vector in the direction of the tangential relative velocity vector at the contact point. The normal and tangential contact forces at the contact points are used to define the generalised contact forces associated with the tyre mesh nodal coordinates. An illustration of the contact force model used in this study is shown in Figure 12.

Figure 12 Contact forces (see online version for colours)

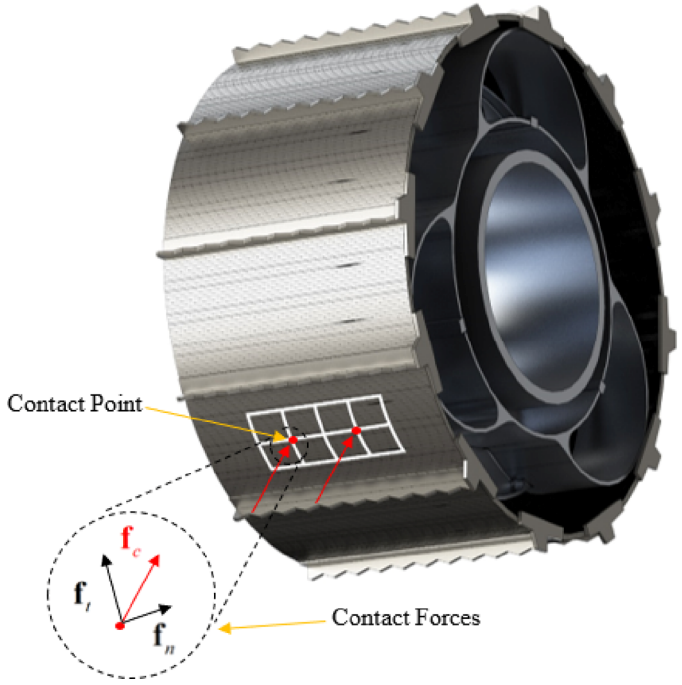

5.2 *Tractive forces*

In general, the tractive forces, which influence the energy consumptions of planetary rovers, depend on the tangential friction forces as well as other forces such as the wind resistance. In this paper, the focus will be mainly on the tyre tangential friction forces in order to compare between the discrete brush and continuum-based ANCF tyre models. The tractive forces resulting from the wheel/soil contact allow the rover to negotiate rough terrains by moving forward, climbing slopes, and passing over obstacles. Wheel slippage and lack of traction can lead to more energy consumption and to deterioration of the performance in the planetary rovers designed to perform sophisticated tasks by following specified motion trajectories. To enhance the low traction of the soft and sandy Mars soil, grousers are often installed on the external surface of the tyre. Increased traction can also be achieved by maximising the wheel/soil contact area. A larger contact patch can be obtained by increasing the wheel diameter (Siddiqi et al., 2006; Schmid, 1995) and/or by using flexible wheels. Due to the mass and dimension constraints that characterise Mars rovers, increasing the wheel dimensions may not be a feasible option. An alternative is to use flexible metal wheels or pneumatic tyres. In general, pneumatic tyres (Meirion-Griffith et al., 2011; Irani et al., 2011; Ding et al., 2011a, 2011b) are avoided in the design of planetary rovers due to risk of tyre puncture, which could compromise the space mission success. Furthermore, pneumatic tyres can become brittle at the low Mars-temperatures. Use of flexible metal wheels presents the only effective option that allows for having a large contact patch, reducing slipping, and avoiding sinkage (Ding et al., 2014; Petersen and McPhee, 2011). Several models were developed in the literature to characterise the wheel/soil contact. Bauer et al.

(2005a, 2005b) and Scharringhausen et al. (2009) developed rigid wheels for rover applications. Peterson et al. (2011) studied a volumetric contact modelling approach for determining closed-form expressions for the rover tyre contact forces. A rigid wheel model that considers slip sinkage was developed by Ding et al. (2014). Flexible wheels were also discussed by different authors (Ishigami et al., 2011; Petersen et al., 2011). Favaedi et al. (2011) predicted the tractive performance of planetary rovers, considering a geometry model of the wheel under deformation. Wang et al. (2019) presented a model for the interaction between a flexible metal wheel and deformable terrain and analysed sinkage and drawbar pull in rover applications.

In this paper, the rover tractive forces are examined using both brush and ANCF airless tyres. The brush tyre/soil contact is described in detail in the literature (Gipser, 2005; Lugner et al., 2005; Pacejka, 2006). The contact between the ANCF wheel and the rigid ground is determined as previously discussed in this section using a penalty approach. The normal force is used to determine the tangential friction force that enters into the formulation of the tractive forces. For ANCF airless tyres, a point mesh is created on each element and this mesh is used to determine the tyre/terrain contact points using a search algorithm. The relative velocities at the contact points are determined, and if this relative velocity is different from zero the friction force at this contact point is computed and applied. It is, however, important to point out that in the steady-state motion, the relative displacement between the tyre and the ground is predominantly rolling. In the case of a flexible tyre, the oscillations of the material points can lead to change in the direction of the relative velocity because in the case of predominant rolling, the slip is small. In a later section of this paper, the tangential friction forces predicted using the brush and ANCF tyres are compared in an acceleration scenario along a straight path.

6 Geometry/analysis integration

Successful geometry/analysis integration is necessary for having a science-based computer-aided engineering (CAE) process for the virtual prototyping and design of space vehicles. As discussed in Section 4, use of ANCF finite elements allows developing a unified geometry/analysis mesh and avoiding the costly, time-consuming, and error-prone process of converting CAD solid models to FE analysis meshes. In this investigation, one computational environment is used for the geometry and analysis steps, and therefore, the CAD/FE mesh conversion is avoided. In this computational environment, the geometry/analysis mesh is first developed and new concepts, such as the ANCF reference nodes, are used in the model assembly. The geometric, material, and reference configuration data of the assembled mesh are defined and used as input to the MBS algorithm that constructs and numerical solves the rover DAE systems. The use of this new geometry/analysis approach allows for eliminating a large number of dependent coordinates before the start of the nonlinear dynamic simulations.

6.1 Reference-configuration geometry and elastic forces

Because of the use of the fully-parameterised plate element, a general continuum mechanics approach can be used for defining the tyre elastic forces. The virtual work of

the tyre elastic forces can be written for an arbitrary element in the geometry/ analysis mesh as $\delta W_s = -\int_{V_o} \boldsymbol{\sigma}_{P2} : \delta\boldsymbol{\varepsilon} dV_o = -\mathbf{Q}_s^T \delta\mathbf{e}$, where V_o is the element volume in the reference configuration, $\boldsymbol{\sigma}_{P2}$ is the second Piola-Kirchhoff stress tensor, $\boldsymbol{\varepsilon}$ is the Green-Lagrange strain tensor, and $\mathbf{Q}_s$ is the vector of generalised elastic forces (Shabana, 2018). As previously discussed, the stress-free reference-configuration of the tyre is accounted for using the form of Green-Lagrange strain tensor $\boldsymbol{\varepsilon} = (1/2)\left[\left(\mathbf{J}_o^{-1}\right)^{\mathrm{T}} \mathbf{J}_e^{\mathrm{T}} \mathbf{J}_e \mathbf{J}_o^{-1} - \mathbf{I}\right]$, where the matrices that appear in this equation are as previously defined in this paper. The vector of elastic force $\mathbf{Q}_s$ is introduced to the equations of motion in the generalised force vector associated with the ANCF nodal coordinates.

6.2 Constrained dynamic equations

Nonlinear constraint equations which cannot be eliminated at the preprocessing stage are formulated using a set of algebraic equations that can be written in a vector form as $\mathbf{C}(\mathbf{q}_r, \mathbf{p}, t) = \mathbf{0}$, where $\mathbf{q}_r$ is the vector of coordinates of the rigid bodies in the rover system, $\mathbf{p}$ is the vector of coordinates of the ANCF bodies, and t is time. The vector of nonlinear constraint equations $\mathbf{C}(\mathbf{q}_r, \mathbf{p}, t) = \mathbf{0}$ that describes mechanical joints and specified motion trajectories can be combined with the second-order differential equations of motion using the vector of Lagrange multipliers $\boldsymbol{\lambda}$. To this end the vector of constraint equations $\mathbf{C}(\mathbf{q}_r, \mathbf{p}, t) = \mathbf{0}$ is differentiated twice with respect to time to obtain $d^2\mathbf{C}/dt^2 = \mathbf{0}$. This equation leads to

$$\mathbf{C}_{\mathbf{q}_r} \ddot{\mathbf{q}}_r + \mathbf{C}_{\mathbf{p}} \ddot{\mathbf{p}} = \mathbf{Q}_c \tag{6}$$

In this equation, $\mathbf{Q}_c$ is the vector that absorbs terms which are not linear in the accelerations and result from differentiating the constraint equations twice with respect to time. Using the preceding equation, one can write the augmented form of the equations of motion as (Shabana, 2020)

$$\begin{bmatrix} \mathbf{M}_r & \mathbf{0} & \mathbf{C}_{\mathbf{q}_r}^{\mathrm{T}} \\ \mathbf{0} & \mathbf{M}_p & \mathbf{C}_{\mathbf{p}}^{\mathrm{T}} \\ \mathbf{C}_{\mathbf{q}_r} & \mathbf{C}_{\mathbf{p}} & \mathbf{0} \end{bmatrix} \begin{bmatrix} \ddot{\mathbf{q}}_r \\ \ddot{\mathbf{p}} \\ \boldsymbol{\lambda} \end{bmatrix} = \begin{bmatrix} \mathbf{Q}_r \\ \mathbf{Q}_p \\ \mathbf{Q}_c \end{bmatrix} \tag{7}$$

In this equation, $\mathbf{M}_r$ and $\mathbf{M}_p$ are the mass matrices associated with the rigid-body and ANCF coordinates, respectively; and $\mathbf{Q}_r$ and $\mathbf{Q}_p$ are the force vectors associated, respectively, with the rigid-body and ANCF coordinates. The tyre/terrain contact forces are introduced to the dynamic formulation as generalised forces in the vector $\mathbf{Q}_p$.

6.3 Computational considerations

In the preceding equation, the mass matrix $\mathbf{M}_p$ and the force vector $\mathbf{Q}_p$ are the mass matrix and force vector of the geometry/analysis mesh obtained for the rover tyre assembly. Therefore, in this investigation, all the rover tyres are treated as one subsystem that has one inertia matrix and one force vector. In the numerical implementation, the

ANCF Cholesky coordinates are used in order to obtain an identity generalised mass matrix, that is, $\mathbf{M}_p = \mathbf{I}$ and the vector $\mathbf{p}$ is the vector of ANCF Cholesky coordinates (Shabana, 2018). This ensures that the coefficient matrix in the augmented Lagrangian equation is a sparse matrix; allowing for using sparse matrix techniques to obtain an efficient solution. The preceding augmented Lagrangian equation is solved for the vectors of accelerations $\ddot{\mathbf{q}}_r$ and $\ddot{\mathbf{p}}$ as well as the vector of Lagrange multipliers $\boldsymbol{\lambda}$. The independent accelerations are identified and integrated forward in time to determine the coordinates and velocities. The MBS numerical algorithm used in this investigation to solve the Mars rover equations is designed to ensure that all the nonlinear constraint equations $\mathbf{C}(\mathbf{q}_r, \mathbf{p}, t) = \mathbf{0}$ are satisfied at the position, velocity, and acceleration levels.

7 Numerical results

In this section, several tests are performed in order to evaluate the accuracy and efficiency of the geometry/analysis approach used in this study to solve the rover nonlinear dynamic equations. Two different rover models are considered in this numerical study. In the first model, the rover tyres are modelled using the discrete brush-type approach, while in the second model, continuum-based ANCF tyres are used. The simulations are performed using the general-purpose MBS software Sigma/Sams (**S**ystematic **I**ntegration of **G**eometric **M**odelling and **A**nalysis for the **S**imulation of **A**rticulated **M**echanical **S**ystems). Because it was not possible for the authors to obtain the exact measurements and material properties of the components of the Mars rover considered in this study, all the numerical results presented in this section should be interpreted as a qualitative assessment of the rover dynamic behaviour and as qualitative comparison between the two tyre models considered in this investigation.

Table 1 Rover inertia properties

Body number	*Component*	*Mass* (kg)	I_{xx} (kg·m^2)	I_{yy} (kg·m^2)	I_{zz} (kg·m^2)
1	Principal body	246.39796	51	65	98
2, 3, 4, 5, 6, 7	Wheel	4.44157	0.05941	0.08571	0.05941
8, 9, 10, 11, 12, 13	Spindle	4.27728	0.14314	0.12524	0.04277
14, 15, 16, 17, 18, 19	Arm	1.74699	0.01933	0.00691	0.01769
20, 21	Pivot lateral right	2.53122	0.00459	0.09341	0.09112
22	Pivot rear	5.74456	0.97106	1.07547	0.11176
23	Ground	0	0	0	0

7.1 Rover model description

Figure 13 shows the components of the wheeled robot used in this numerical investigation. The inertia properties of different components are provided in Table 1, where I_{xx}, I_{yy}, and I_{zz} are the mass moments of inertia. The mass of the vehicle is

approximately 320 kg. The actuators are defined using 21 revolute joints. Figure 14 shows the connections of different components in one of the bogie structures of the vehicle. The weight distribution among different wheels is calculated using static equilibrium analysis, as shown in Figure 15.

Figure 13 Components of the rover (see online version for colours)

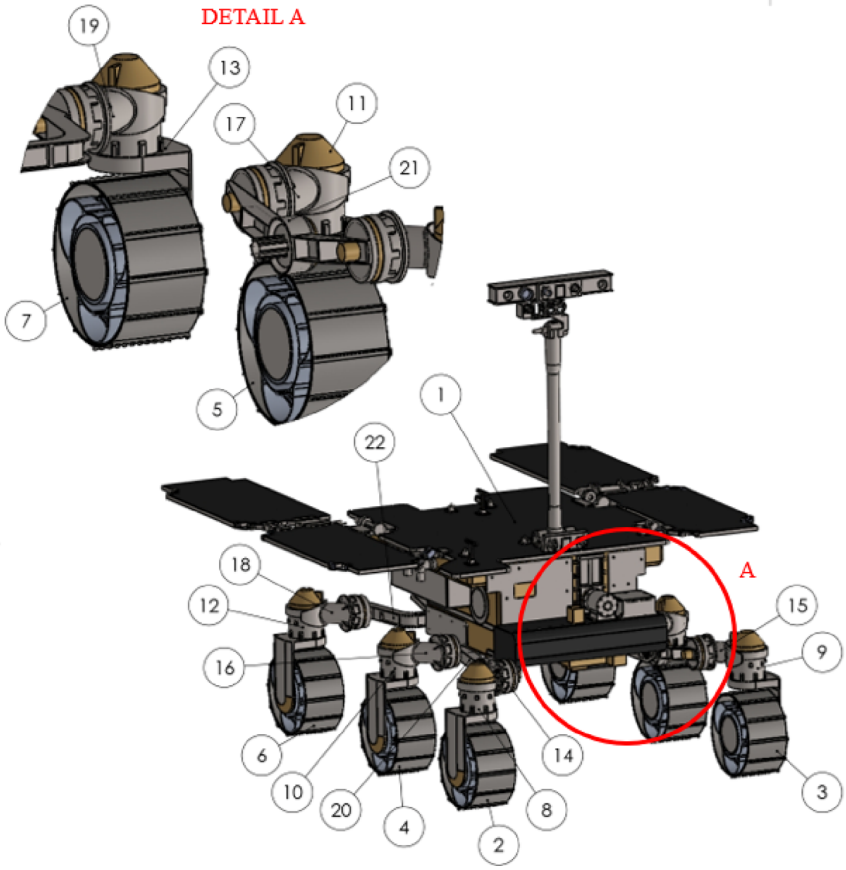

7.2 *Brush-type rover model*

In this first numerical example, the wheels are defined using a discrete brush-type model which does not account for the distributed inertia and elasticity. The initial system configuration is depicted in Figure 16. For the purpose of verifying the results obtained in this numerical investigation, the average stiffness curve obtained by Sivo et al. (2019) and shown in Figure 17 is considered. As previously mentioned, because of the rover wheel configuration, the radial stiffness of the wheel varies along the circumferential direction. If a brush-type tyre model is used, this radial stiffness variation cannot be easily captured because of the simplicity of the approach. For this reason, the results can only be verified against an average stiffness curve. In the first dynamic simulation scenario performed, a free fall of the rover on the ground, starting from a height of 10 mm, is considered. For each wheel, the force acting on the wheel centre of mass and

the wheel deformation are measured. The wheel normal contact forces and radial deformations are shown in Figures 18 and 19, respectively. The results shown in Figure 18 are in agreement with the results obtained using a static analysis. The brush tyre stiffness and damping coefficients are defined using a tuning procedure while the friction and rolling resistance coefficients are defined according to Zhou et al. (2013) and are shown in Table 2. The vertical force acting on the principal body of the rover was gradually increased, so that each wheel would be subjected to a normal load in the range of 160 – 250 N. The results obtained are compared with the reference numerical results of Sivo et al. (2019), as shown in Figure 20. It is observed that the brush-type tyre results match the reference results only when small deformations are considered. As the load increases, the brush-type wheel model fails to capture the material and geometric nonlinearities. Because the rover wheels experience, in general, large deformations, it is clear that the discrete brush-type approach cannot be used to produce accurate results.

Figure 14 Rover revolute joints (see online version for colours)

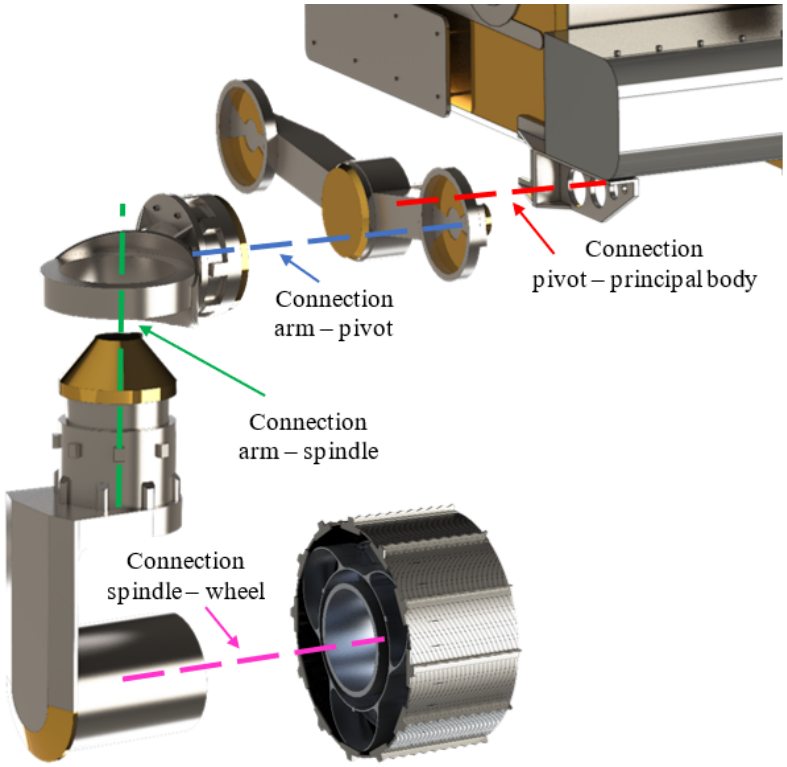

7.3 ANCF airless tyres

Using the ANCF approach, each tyre is modelled as a simple cylinder with four radial elements. The wheel mesh consists of eight fully-parameterised plate elements and one ANCF reference node rigidly connected to the eight internal nodes of the rigid inner hub. The material properties are defined as density $\rho = 1500$ kg/m^3, Young modulus $E = 28{,}000$ Pa, and Poisson ratio $\nu = 0$. Material damping is introduced using the

approach proposed by Grossi and Shabana (2019). The stiffness, damping, and friction coefficients used in the contact force model are defined as $k = 1000$ N/m, $c = 100$ Ns/m and $\mu = 0.6$, respectively. The initial configuration of the rover with the ANCF wheels is shown in Figure 21. The reference results for this analysis are shown in Figure 7. Following a similar procedure to what described in the previous section, two different force-deformation curves are found. These two different curves, shown in Figure 22, are associated with different circumferential orientations of the wheel. It is clear that the two curves are in good agreement with the reference results.

Figure 15 Weight distribution on the rover wheels (see online version for colours)

Normal Force	**Value** (N)
Front	177.6
Middle	177.7
Rear	238.2

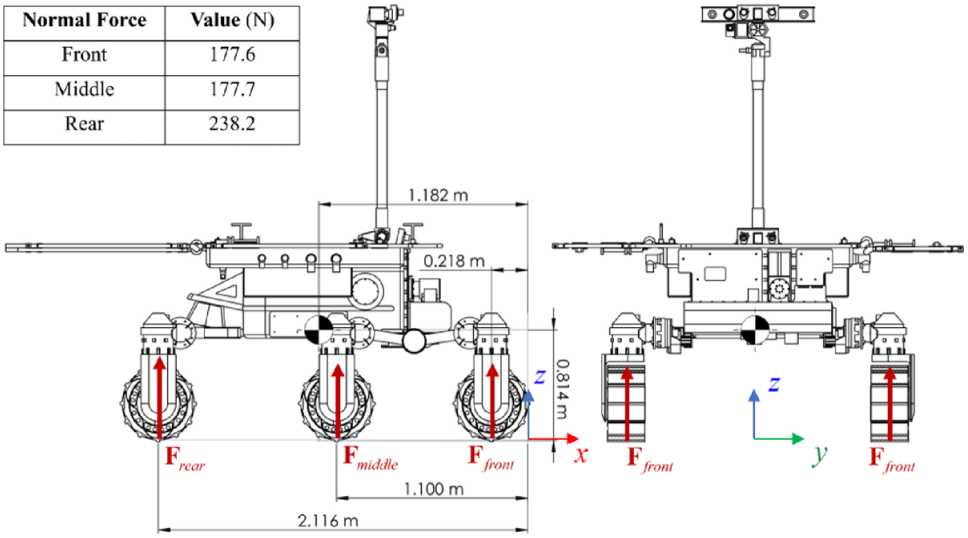

Figure 16 Rover model with the brush-type tyres (see online version for colours)

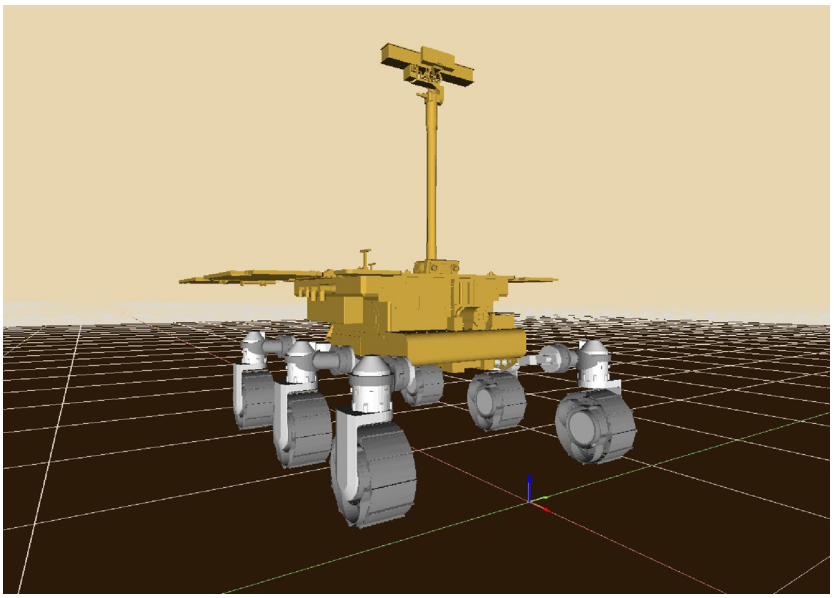

Figure 17 Average stiffness curve (Sivo et al., 2019) (see online version for colours)

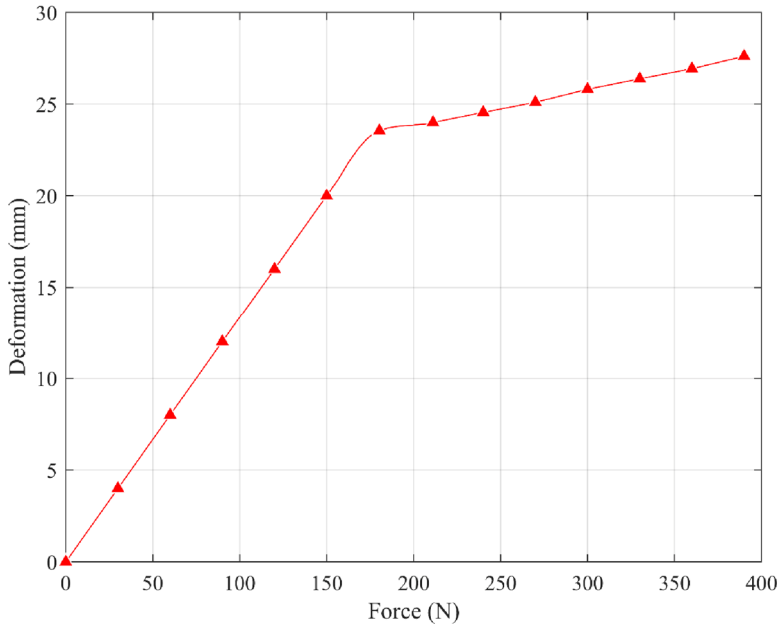

Figure 18 Vertical force on a brush-type tyre in the free fall scenario (see online version for colours)

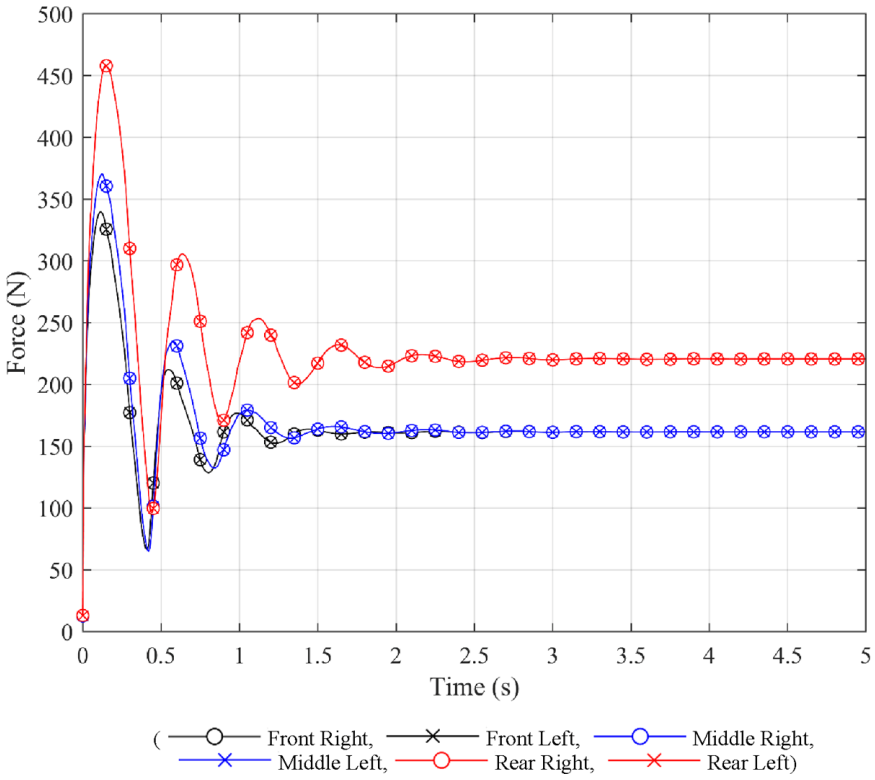

Figure 19 Deformation of a brush-type tyre in the free fall scenario (see online version for colours)

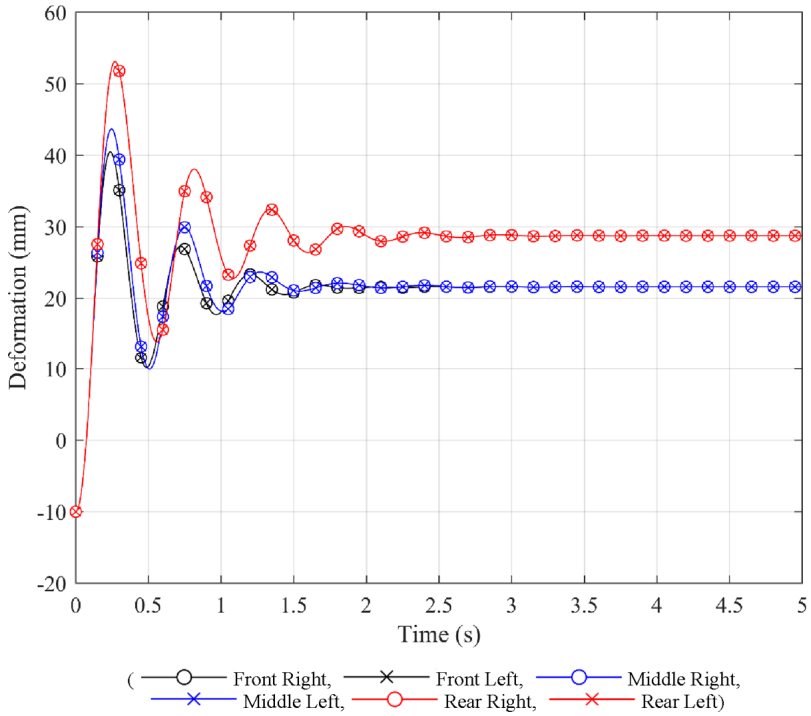

Figure 20 Verification of the brush-type tyre model (see online version for colours)

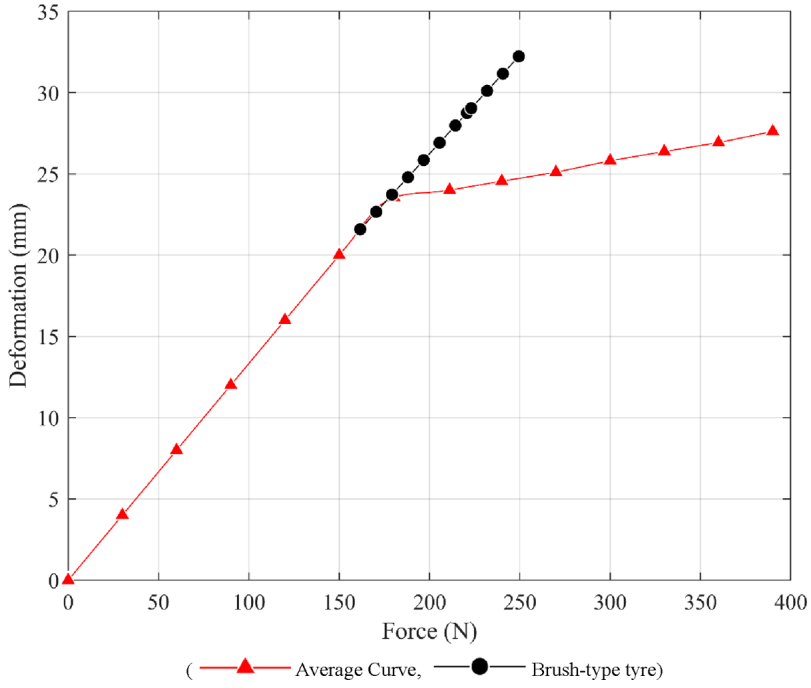

Figure 21 Rover model with ANCF airless tyres (see online version for colours)

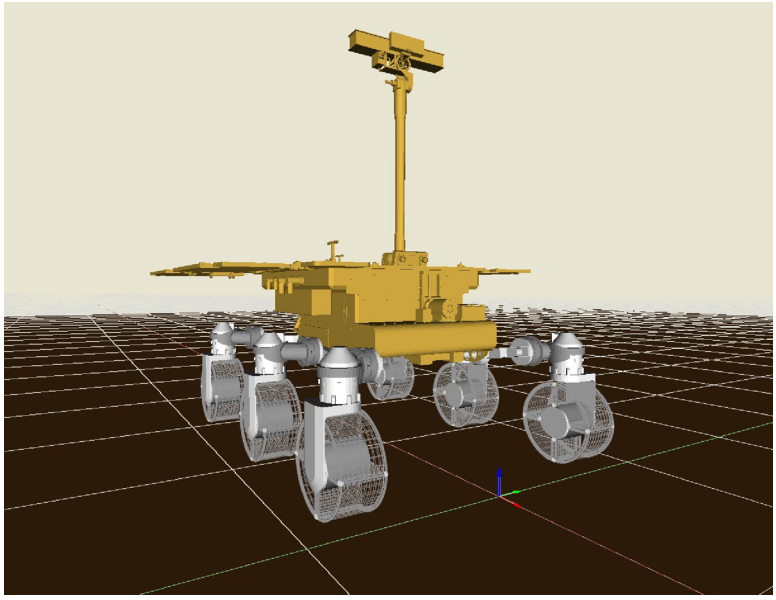

Figure 22 Verification of the ANCF airless tyre (see online version for colours)

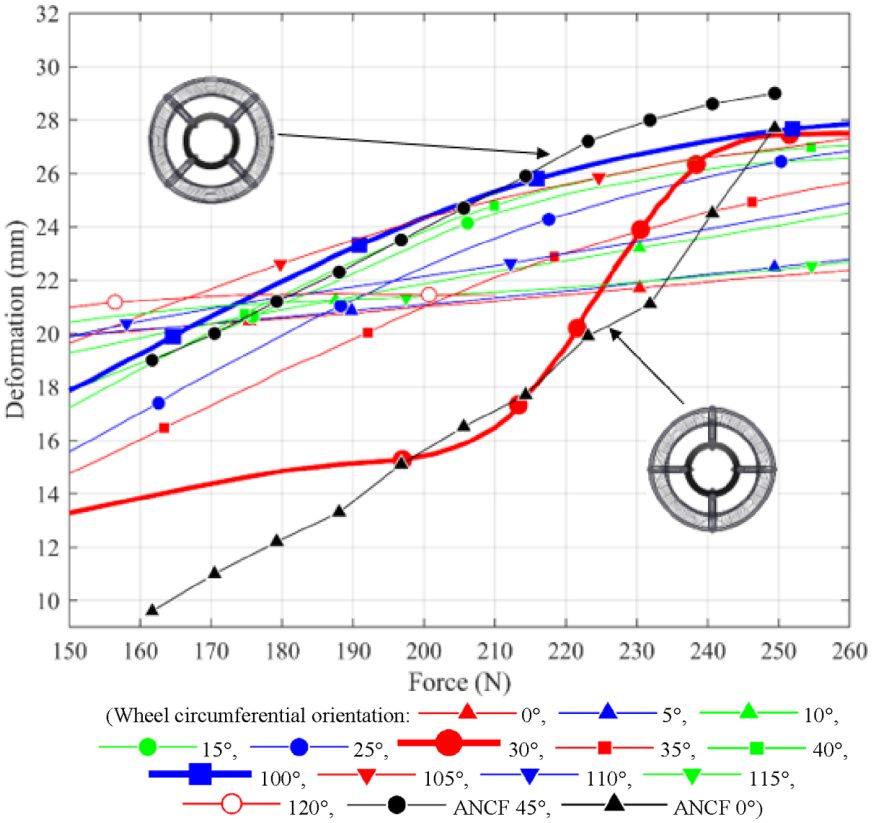

Table 2 Brush-type tyre parameters

Parameter	*Value*
Radial stiffness (N/m)	8250
Radial damping (N·s/m)	8140
Longitudinal slip stiffness (N/m^2)	8250
Lateral slip stiffness (N/deg·m^2)	850
Minimum friction coefficient	0.597
Maximum friction coefficient	0.757
Rolling resistance coefficient	0.015

Figure 23 Forward velocity of the principal body

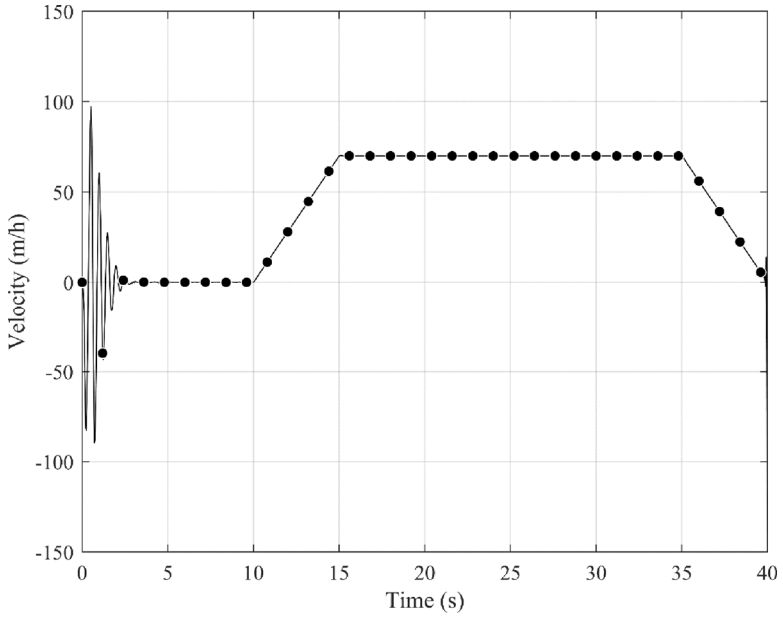

7.4 Comparative study

The two MBS rover models considered in this section have identical data except for the wheel modelling approach used. In the first rover model, the discrete brush-type model is used, while in the second approach the continuum-based ANCF model is used. In order to compare between the two models in a dynamic motion scenario, the rover is assumed to negotiate a straight path by reaching its average locomotion speed of 70 m/h. The vehicle is dropped on the ground and allowed to reach its static equilibrium configuration. Subsequently, angular velocity constraints are applied to each wheel, to initiate the forward motion of the vehicle. The vehicle accelerates for 5 s until the desired velocity is reached. The overall computer simulation of 40 s includes also a deceleration of the rover during the last 5 s. The forward velocity of the principal body during the simulation is shown in Figure 23. Figure 24 shows the deformation of the right wheel for the two tyre models, in the interval of time between 15 s and 35 s. It is observed that the

brush-type wheel behaves identically for all the circumferential positions, thus resulting in a constant deformation. On the other hand, the ANCF-wheel deformation changes as function of the circumferential orientation. This behaviour is expected because the radial stiffness of the ANCF wheel varies depending on the wheel orientation. While there is still room for further improvements and algorithm optimisation to enhance the computational efficiency of the ANCF rover model, this computational time is still significantly lower than what was reported in the literature for similar models (Sivo et al., 2019).

Figure 24 Comparison between brush-type and ANCF airless tyres (see online version for colours)

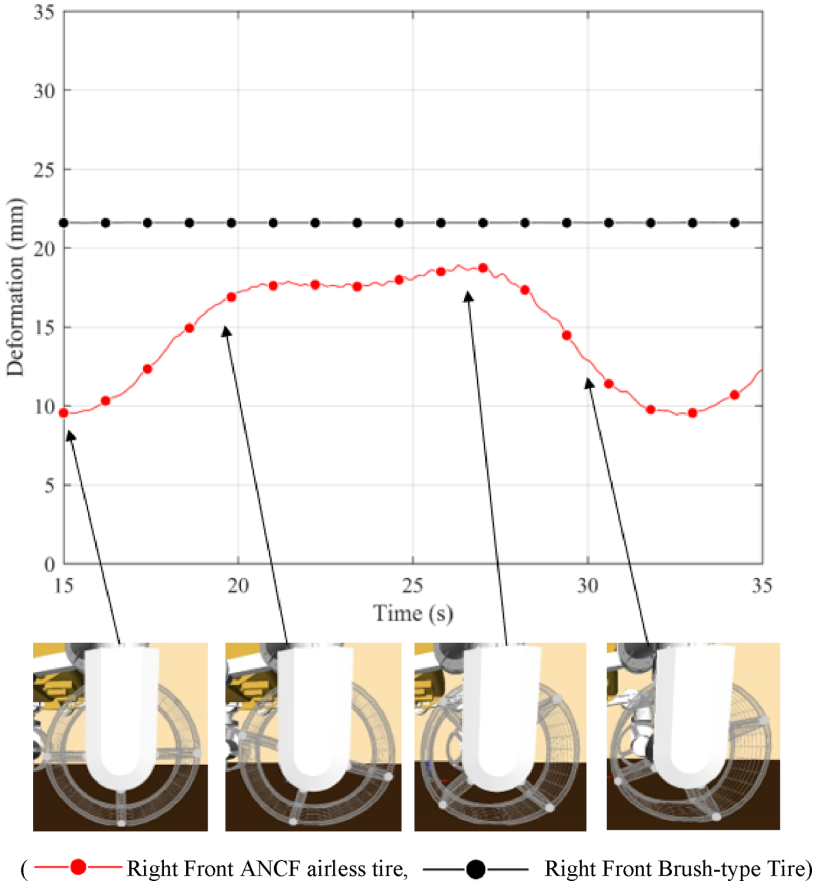

7.5 Tractive force

The tractive forces are examined in this numerical investigation using the two MBS rover models of Section 7.4; the first model consists of 6 brush-type tyres, while the second model consists of six ANCF tyres. A constant driving moment $M_T = 3.5$ N·m is applied to each wheel for 10 s, in order to have the same dynamic conditions applied to the two tyre types. The contact between the rigid ground and the ANCF tyres is predicted using a grid of 100 points on the surface of each ANCF plate element. The total tractive force on each ANCF tyre is computed as the sum of the tractive forces calculated at each contact point.

The dynamic friction coefficient used in the calculation of the tractive forces is $\mu = 0.6$. Figure 25 compares the tractive forces of the front-right wheel obtained with the brush-type and ANCF models. During the first 5 s, the rover reaches equilibrium on the ground and starts accelerating under the effect of the driving moments. It is observed that the ANCF tyre, because of its flexibility, captures the oscillatory nature of the tangential friction force which is not captured by the discrete brush-type tyre. The oscillations in the ANCF friction forces are due to localised slippage occurring in the contact patch. The use of ANCF tyres also allows for capturing high frequency localised oscillations resulting from the tyre/soil interaction. Such high frequency oscillations, which cannot be captured using simplified tyre models such as the brush-type tyre, are important for performing accurate durability; and noise, vibration and harshness (NVH) investigations.

Figure 25 Tractive force (see online version for colours)

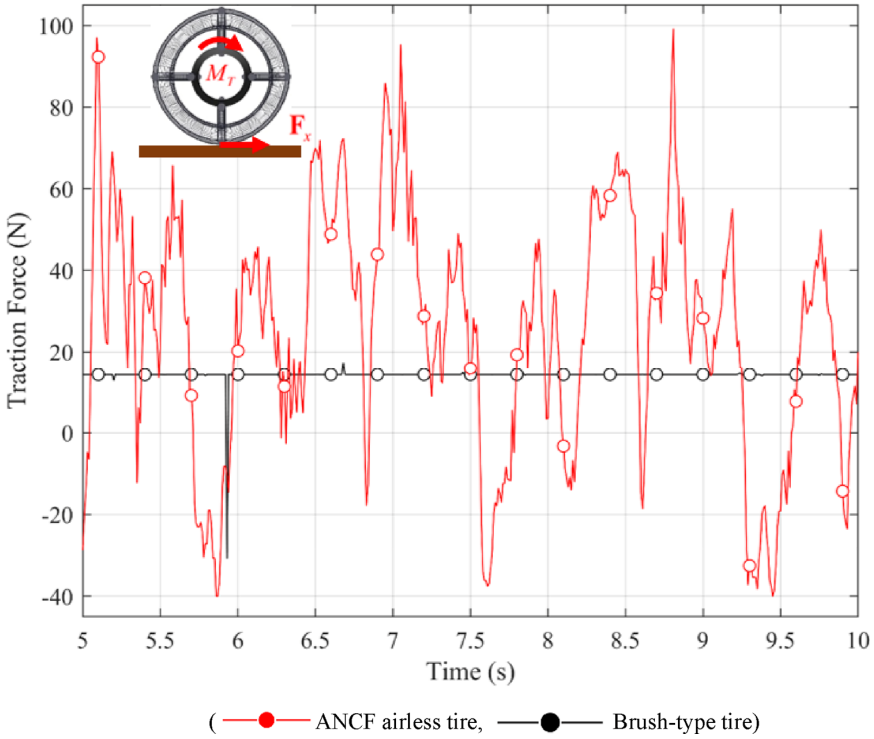

8 Summary and conclusions

This paper describes a geometry/analysis approach for the virtual prototyping of wheeled robots used in the space-exploration missions. Because of the scientific challenges of space explorations, some international space agencies are teaming up to design autonomous wheeled robots such as the Mars rover considered in this study. The Mars rovers, designed as wheeled robots, collect terrain information, including dust, soil, rocks, and liquids. This paper describes a computational framework that can be used for both geometry and analysis to avoid the conversion of CAD solid models to analysis

meshes and to significantly reduce reliance on physical prototyping which is costly and time-consuming. A computational MBS approach is used to construct and numerically solve the rover DAEs. A unified analysis/geometry mesh of the rover *airless wheels*, that can adapt to different soil patterns and harsh operating and environmental conditions without the puncture risk of pneumatic tyres, is developed using fully-parameterised ANCF plate elements. The degree of the matrix sparsity in the constrained-dynamics approach used to solve the nonlinear dynamic equations of the MBS rover model is increased by using the ANCF Cholesky coordinates which lead to a generalised identity inertia matrix. Several simulation scenarios are considered, including a drop test and acceleration along a straight line. The numerical results obtained are verified using data published in the literature and are used to evaluate the accuracy and computational efficiency of the ANCF airless-tyre modelling approach. The results obtained using the continuum-based ANCF tyre model are also compared with the results of the discrete brush-type tyre model.

Acknowledgements

This research was supported in part by the National Science Foundation (Project # 1852510).

References

Bauer, R., Leung, W. and Barfoot, T. (2005a) 'Development of a dynamic simulation tool for the exomars rover', *The 8th International Symposium on Artificial Intelligence*, *Robotics and Automation in Space (iSAIRAS)*, Munich, Germany.

Bauer, R., Leung, W. and Barfoot, T. (2005b) 'Experimental and simulation results of wheel-soil interaction for planetary rovers', *Proceedings of IEEE/ RSJ International Conference on Intelligent Robots and Systems (IROS)*, Edmonton, Canada, pp.586–591.

Ding, L., Deng, Z., Gao, H., Nagatani, K. and Yoshida, K. (2011a) 'Planetary rovers' wheel-soil interaction mechanics: new challenges and applications for wheeled mobile robots', *Intel Serv Robotics*, Vol. 4, pp.17–38.

Ding, L., Gao, H., Deng, Z. and Tao, J. (2011b) 'Wheel slip-sinkage and its estimation model of lunar rover', *J. Cent. South Univ. Technol.*, Vol. 17, No. 1, pp.129–135.

Ding, L., Gao, H., Deng, Z., Tao, J., Iagnemma, K. and Liu, G. (2014) 'Interaction mechanics model for rigid driving wheels of planetary rovers moving on sandy terrain with consideration of multiple physical effects', *J. Field Robot*, Vol. 32, No. 6, pp.827–859.

Farin, G. (2002) *Curves and Surfaces for CAGD, A Practical Guide*, 5th ed., Morgan Kaufmann, Publishers, San Francisco.

Favaedi, Y., Pechev, A., Scharringhausen, M. and Richter, L. (2011) 'Prediction of tractive response for flexible wheels with application to planetary rovers', *J. Terramechanics*, Vol. 48, No. 3, pp.199–213.

Fotland, G., Haskins, C. and Rølvåg, T. (2019) 'Trade study to select best alternative for cable and pulley simulation for cranes on offshore vessels', *Systems Engineering*, pp.1–12, DOI: 10.1002/sys.21503.

Gallier, J. (2011) *Geometric Methods and Applications: For Computer Science and Engineering*, Springer, New York.

Gipser, M. (2005) 'FTire: a physically based application-oriented tyre model for use with detailed MBS and finite-element suspension models', *Veh. Syst. Dyn*., Vol. 43, No. 1, pp.76–91.

Goetz, A. (1970) *Introduction to Differential Geometry*, Addison Wesley, Boston.

Grossi, E. and Shabana, A.A. (2019) 'Analysis of high-frequency ANCF modes: Navier-Stokes physical damping and implicit numerical integration', *ActaMechanica*, Vol. 230, No. 7, pp.2581–2605.

Grossi, E., Desai, C.J. and Shabana, A.A. (2019) 'Development of geometrically accurate continuum-based tire models for virtual testing', *Journal of Computational and Nonlinear Dynamics*, Vol. 14, pp.121006-1–121006-11.

He, G., Patel, M. and Shabana, A.A. (2017) 'Integration of localized surface geometry in fully parameterized ANCF finite elements', *Comput. Methods Appl. Mech. Eng*., Vol. 313, pp.966–985.

Hu, W., Tian, Q. and Hu, H.Y. (2014) 'Dynamics simulation of the liquid-filled flexible multibody system via the absolute nodal coordinate formulation and SPH method', *Nonlinear Dynamics*, Vol. 75, pp.653–671.

Ishigami, G., Otsuki, M., Kubota, T. and Iagnemma, K. (2011) 'Modeling of flexible and rigid wheels for exploration rover on rough terrain', *Proceedings of the 28th International Symposium on Space Technology and Science*, pp.1–6.

Johnson, J., Kulchitsky, A., Duvoy, P., Iagnemma, K., Senatore, C., Arvidson, R. and Moore, J. (2015) 'Discrete element method simulations of Mars Exploration Rover wheel performance', *Journal of Terramechanics*, Vol. 62, pp.31–40.

Knuth, M.A., Johnson, J.B., Hopkins, M.A., Sullivan, R.J. and Moored, J.M. (2012) 'Discrete element modeling of a Mars exploration rover wheel in granular material', *Journal of Terramechanics,* Vol. 49, No. 1, pp.27–36.

Kreyszig, E. (1991) *Differential Geometry*, Dover Publications, Toronto, Canada.

Liu, C., Tian, Q. and Hu, H.Y. (2011) 'Dynamics of large scale rigid-flexible multibody system composed of composite laminated plates', *Multibody System Dynamics*, Vol. 26, pp.283–305.

Lugner, P., Pacejka, H. and Plöchl, M. (2005) 'Recent advances in tyre models and testing procedures', *Veh. Syst. Dyn*., Vol. 43, Nos. 6–7, pp.413–426.

Ma, C., Wang, R., Wei, C. and Zhao, Y. (2016) 'A new absolute nodal coordinate formulation of solid element with continuity condition and viscosity model', *International Journal of Simulation: Systems, Science and Technology*, Vol. 17, No. 21, pp.10.1–10.6.

Ma, L., Wei, C. and Zhao, Y. (2020) 'Modeling and verification of a RANCF fluid element based on cubic rational Bezier volume', *ASME Journal of Computational and Nonlinear Dynamics*, Vol. 15, No. 4, pp.04-1005–04-1020.

Nachbagauer, K. (2014) 'State of the art of ANCF elements regarding geometric description, interpolation strategies, definition of elastic forces, validation and locking phenomenon in comparison with proposed beam finite elements', *Archives of Computational Methods in Engineering*, Vol. 21, No. 3, pp.293–319.

Obrezko, L.P., Matikainen, M.K. and Harish, A.B. (2020) 'A finite element for soft tissue deformation based on the absolute nodal coordinate formulation', *ActaMechanica*, https://doi.org/10.1007/s00707-019-02607-4

Orzechowski, G. and Fraczek, J. (2015) 'Nearly incompressible nonlinear material models in the large deformation analysis of beams using ANCF', *Nonlinear Dynamics*, Vol. 82, No. 1, pp.451–464.

Pacejka, H.B. (2006) *Tyre and Vehicle Dynamics*, 2nd ed., Elsevier, Oxford, England.

Pappalardo, C.M., Biondo, A., Oliva, A. and Guida, D. (2020) 'A general method for performing an integrated CAD-MBD-FE analysis', in Tonkonogyi, V. (Ed.): *Advanced Manufacturing Processes, InterPartner-2019*, LNME, Springer, pp.264–272.

Pappalardo, C.M., Wallin, M. and Shabana, A.A. (2017) 'A new ANCF/CRBF fully parameterized plate finite element', *ASME J. Comput. Nonlinear Dyn*., Vol. 12, No. 3, p.031008.

Patel, M., Orzechowski, G., Tian, Q. and Shabana, A.A. (2016) 'A new multibody system approach for tire modeling using ANCF finite elements', *Proc. Inst. Mech. Eng., Part K*, Vol. 230, No. 1, pp.69–84.

Patel, M.D., Pappalardo, C.M., Wang, G. and Shabana, A.A. (2019) 'Integration of geometry and small and large deformation analysis for vehicle modelling: chassis, and airless and pneumatic tyre flexibility', *Int. J. Veh. Perform*., Vol. 5, No. 1, pp.90–127.

Petersen, W. and McPhee, J. (2011) 'A study of volumetric contact modelling approaches in rigid tire simulation for planetary rover application', *International Journal of Vehicle Design*, Vol. 64, Nos. 2–4, pp.262–279.

Petersen, W., Vyasarayani, C.P. and Mcphee, J. (2011) 'Flexible planetary rover tire model with volumetric wheel/soil interface', *17th International Conference of the International Society for Terrain-Vehicle Systems*, pp.473–480.

Piegl, L. and Tiller, W. (1997) *The NURBS Book*, 2nd ed., Springer, Berlin.

Poulakis, P., Vago, J.L., Loizeau, D., Vicente-Arevalo, C., Hutton, A., McCoubrey, R., Arnedo-Rodriguez, J., Smith, J., Boyes, B., Jessen, S., Otero-Rubio, A., Durrant, S., Gould, G., Joudrier, L., Yushtein, Y., Alary, C., Zekri, E., Baglioni, P., Cernusco, A., Maggioni, F., Yague, R. and Ravera, F. (2015) 'Overview and development status of the ExoMars rover mobility subsystem', *13th ESA Workshop on Advanced Space Technologies for Robotics and Automation*, Noordwjk, The Netherlands.

Rogers, D.F. (2001) *An Introduction to NURBS with Historical Perspective*, Academic Press, San Diego, CA.

Scharringhausen, M., Beermann, D., Krömer, O. and Richter, L. (2009) 'A Wheel-soil interaction model for planetary application', *11th European Regional Conference on Terrain-Vehicle Systems (ISTVS 2009)*, Bremen, Germany.

Schmid, I.C. (1995) 'Interaction of vehicle and terrain results from 10 years research at IKK', *Journal of Terramechanics*, Vol. 32, No. 1, pp.3–26.

Shabana, A.A. (2014) 'ANCF reference node for multibody system applications', *IMechE J. Multibody Dyn.*, Vol. 229, No. 1, pp.109–112.

Shabana, A.A. (2015) 'ANCF tire assembly model for multibody system applications', *ASME J. Comput. Nonlinear Dyn*., Vol. 10, No. 2, p.024504.

Shabana, A.A. (2018) *Computational Continuum Mechanics*, 3rd ed., John Wiley and Sons, Chichester, UK.

Shabana, A.A. (2019) 'Integration of computer-aided design and analysis (I-CAD-A): application to multibody vehicle systems', *International Journal of Vehicle Performance*, Vol. 5, pp.300–327.

Shabana, A.A. (2020) *Dynamics of Multibody Systems*, 5th ed., Cambridge University Press, Cambridge.

Shen, Z., Li, P., Liu, C. and Hu, G. (2014) 'A finite element beam model including cross-section distortion in the absolute nodal coordinate formulation', *Nonlinear Dynamics*, Vol. 77, No. 3, pp.1019–1033.

Siddiqi, A., Weck, O. and Iagnemma, K. (2006) 'Reconfigurability in planetary surface vehicles: modelling approaches and case study', *J. Brit. InterplanetSoc.*, Vol. 59, No. 1, pp.450–460.

Sivo, S., Stio, A., Mocera, F. and Somà, A. (2019) 'A study of a rover wheel for martian explorations, based on a flexible multibody approach', *Proc. Inst. Mech. Eng., Part K*, pp.1–16.

Wang, S., Zou, M., Dang, Z., Chen, B., Zhou, T. and Su, B. (2019) 'Modelling of flexible metal wheels for planetary rover on deformable terrain', *Thin-Walled Structures*, Vol. 141, pp.97–110.

Wang, T. (2020) 'Two new triangular thin plate/shell elements based on the absolute nodal coordinate formulation', *Nonlinear Dynamics*, https://doi.org/10.1007/s11071-019-05448-x

Yamano, A.A., Shintani, A., Ito, T., Nakagawa, C. and Ijima, H. (2020) 'Influence of boundary conditions on a flutter-mill', *Sound and Vibration*, Vol. 478, p.115359.

Zhou, F., Arvidson, R.E., Bennett, K., Trease, B., Lindemann, R., Bellutta, P., Iagnemma, K. and Senatore, C. (2013) 'Simulations of Mars rover traverses', *Journal of Field Robotics*, Vol. 31, No. 1, pp.141–160.

Bibliography

Acary, V., Brémond, M., Kapellos, K., Michalczyk, J. and Pissard-Gibollet, R. (2013) 'Mechanical simulation of the exomars rover using Siconos in 3DROV', *12th Symposium on Advanced Space Technologies in Robotics and Automation*, ESA/ESTEC, Noordwijk, Netherlands.

Asnani, V., Delap, D. and Creager, C. (2009) *The Development of Wheels for the Lunar Roving Vehicle*, National Aeronautics and Space Administration, n. 215798.

Bauer, R., Barfoot, T., Leung, W. and Ravindran, G. (2008) 'Dynamic simulation tool development for planetary rovers', *International Journal of Advanced Robotic System*, Vol. 5, No. 3, pp.311–314.

Blundell, M. and Harty, D. (2004) *Multibody Systems Approach to Vehicle Dynamics*, Elsevier, New York.

Chottiner, J.E. (1992) *Simulation of a Six Wheeled Martian Rover Called the Rocker Bogie*, Master's Thesis, The Ohio State University.

Favaedi, Y. and Pechev, A. (2008) 'Development of tractive performance prediction for flexible wheel', *10th ESA Workshop on Advanced Space Technologies for Robotics and Automation*, Noordwijk, Netherlands.

Gajjar, B.I. and Johnson, R.W. (2002) 'Kinematic modeling of terrain adapting wheeled mobile robot for mars exploration', *Third International Workshop on Robot Motion and Control*, pp.291–296.

Garett, S. and Abhinandan, J. (2008) 'Wheel-terrain contact modeling in the ROAMS planetary rover simulation', *Proceedings of the ASME 2005 International Design Engineering Technical Conferences and Computers and Information in Engineering Conference*, Vol. 6, pp.89–97.

Grand, C., Amar, B. and Bidaud, P. (2001) 'A simulation system for behavior evaluation of off-road mobile robots', *Proceedings of the 4th International Conference on Climbing and Walking Robotics*, Karlsruhe, Germany, pp.307–314.

Grand, C., Amar, F.B., Plumet, F. and Bidand, P. (2002) 'Simulation and control of high mobility rovers for rough terrains exploration', *Proceedings of the IARP International Workshop on Humanitarian Demining*, No. 1, pp.51–56.

Hartl, A.E. (2011) *Modeling and Simulation of the Dynamics of Dissipative, Inelastic Spheres with Applications to Planetary Rovers and Gravitational Billiards*, PhD Thesis, North Carolina State University.

Heverly, M. *et al*. (2013) 'Traverse performance characterization for the Mars science laboratory rover', *Journal of Field Robotics*, Vol. 30, No. 6, pp.835–846. **AUTHOR PLEASE SUPPLY REMAINING AUTHOR NAMES.**

Iagnemma, K., Senatore, C., Trease, B., Arvidson, R., Bennett, K., Shaw, A., Zhou, F., Van Dyke, L. and Lindemann, R. (2011) 'Terramechanics modeling of Mars surface exploration rovers for simulation and parameter estimation', *ASME International Design Engineering Technical Conference & Computers and Information Engineering Conference*, IDETC/CIE, pp.805–812.

Jerome, B.J., Kulchitsky, A.V., Duvoy, P., Iagnemma, K., Senatore, C., Arvidson, R.E. and Moored, J. (2015) 'Discrete element method simulations of Mars exploration rover wheel performance', *Journal of Terramechanics*, Vol. 62, pp.31–40.

Krenn, R., Gibbesch, A. and Hirzinger, G. (2006) 'Contact dynamics simulation of rover locomotion', *The 9th International Symposium on Artificial Intelligence*, *Robotics and Automation in Space (iSAIRAS)*, pp.1–8.

Kucherenko, V., Bogatchev, A. and Winnendael, M.V. (2004) 'Chassis concepts for the ExoMars rover', *8th ESA Workshop on Advanced Space Technologies for Robotics and Automation, 'ASTRA 2004'*, Noordwijk, The Netherlands, Vol. c, pp.1–8.

Leite, A.C. and Schäfer, B. (2011) 'On multi-objective optimization of planetary exploration rovers applied to Exomars-type rovers', *ESA/ESTEC*, Noordwijk, Netherlands.

Loizeau, D. (2015) 'ExoMars 2018: the candidate landing sites', *46th Lunar and Planetary Science Conference*, The Woodlands, Texas, USA.

McCoubrey, R. (2014) 'Canada's suspension and locomotion subsystem for ExoMars 2018', *International Astronautics Congress 2014*, Toronto, Canada, pp.3–6.

Mccoubrey, R. (2014) 'ExoMars suspension and locomotion', *iSAIRAS*, Montreal, Canada, pp.4–7.

Nicolini, A., Mocera, F. and Somà, A. (2019) 'Multibody simulation of a tracked vehicle with deformable ground contact model', *ProcIMechE Part K: J Multi-body Dynamics*, Vol. 233, No. 1, pp.152–162.

Patel, N., Slade, R. and Clemmet, J. (2010) 'The ExoMars rover locomotion subsystem', *Journal of Terramechanics*, Vol. 47, No. 4, pp.227–242.

Perez-Davis, M.E. and Gaier, J.R. (1990) *The Chemical Effects of the Martian Environment on Power System Component Materials: A Theoretical Approach*, NASA Technical Memorandum, No. 103203.

Schäfer, B. and Gibbesch, A. (2007) 'Planetary rover mobility: wheel-soil interaction based on multibody system approach', *IFAC Proc*., Vol. 40, pp.883–888.

Shabana, A.A. and Mikkola, A. (2003) 'Use of finite element absolute nodal coordinate formulation in modeling slope discontinuity', *ASME Journal of Mechanical Design*, Vol. 125, No. 2, pp.342–350.

Shabana, A.A. and Zhang, D. (2020) 'ANCF curvature continuity: application to soft and fluid materials', *Nonlinear Dynamics*, Vol. 100, pp.1497–1517.

Stéphane, M., Gibbesch, A., Thüer, T., Krebs, A., Lee, C., Despont, B., Schäfer, B. and Slade, R. (2008) 'Development of the ExoMars chassis and locomotion subsystem', *The 9th International Symposium on Artificial Intelligence, Robotics and Automation in Space (iSAIRAS)*, ETH Library, Research Collection, CA, USA.

Sullivan, R., Anderson, R., Biesiadecki, J., Bond, T. and Stewart, H. (2011) 'Cohesions, friction angles, and other physical properties of Martian Regolith from Mars exploration rover wheel trenches and wheel scuffs', *Journal of Geophysical Research*, Vol. 116, p.E02006.

Vago, J.L. and Westall, F. (2017) 'Pasteur instrument teams, landing site selection working group, and other contributors, 2017) 'Habitability on early Mars and the search for biosignatures with the ExoMars rover', *Astrobiology*, Vol. 17, Nos. 6–7, pp.471–579.

Van Winnendael, M., Baglioni, P. and Vago, J.L. (2005) 'Development of the EsaExomars rover', *The 8th International Symposium on Artificial Intelligence*, *Robotics and Automation in Space (iSAIRAS)*, Munich, Germany.

Wong, J.Y. (2010) *Terramechanics and Off-Road Vehicle Engineering: Terrain Behaviour, Off-Road Vehicle Performance and Design*, Elsevier, Amsterdam, The Netherlands.

Young, A.H. (2007) *Lunar and Planetary Rovers – The Wheels of Apollo and the Quest for Mars*, Springer, Praxis Publishing Chichester.